



1 **Statistical modeling of the long-range dependent structure of barrier island framework**  
2 **geology and surface geomorphology**

3 Bradley A. Weymer<sup>1,2\*</sup>, Phillipe Wernette<sup>3</sup>, Mark E. Everett<sup>2</sup>, Chris Houser<sup>3</sup>

4 <sup>1</sup>GEOMAR - Helmholtz Center for Ocean Research Kiel, Wischhofstraße 1-3, D-24148 Kiel,  
5 Germany

6 <sup>2</sup>Texas A&M University, Department of Geology and Geophysics, College Station, Texas  
7 77843, USA.

8 <sup>3</sup>University of Windsor, Department of Earth and Environmental Sciences, Windsor, Ontario  
9 N9B 3P4, Canada.

10 *Correspondence to:* Bradley A. Weymer ([brad.weymer@gmail.com](mailto:brad.weymer@gmail.com))

11

12

13

14

15

16

17

18

19

20

21

22

23

24

25

26

27

28

29

30

31

32



33 **Abstract**

34 Shorelines exhibit long-range dependence (LRD) and have been shown in some environments to  
35 be described in the wavenumber domain by a power law characteristic of scale-independence.  
36 Recent evidence suggests that the geomorphology of barrier islands can, however, exhibit scale-  
37 dependence as a result of systematic variations of the underlying framework geology. The LRD of  
38 framework geology, which influences island geomorphology and its response to storms and sea  
39 level rise, has not been previously examined. Electromagnetic induction (EMI) surveys conducted  
40 along Padre Island National Seashore (PAIS), Texas, USA, reveal that the EMI apparent  
41 conductivity  $\sigma_a$  signal and, by inference, the framework geology exhibits LRD at scales up to  $10^1$   
42 to  $10^2$  km. Our study demonstrates the utility of describing EMI  $\sigma_a$  and LiDAR spatial series by a  
43 fractional auto-regressive integrated moving average process that specifically models LRD. This  
44 method offers a robust and compact way for quantifying the geological variations along a barrier  
45 island shoreline using three parameters  $(p,d,q)$ . We discuss how ARIMA  $(0,d,0)$  models that use a  
46 single parameter  $d$  provide a quantitative measure for determining free and forced barrier island  
47 evolutionary behavior across different scales. Statistical analyses at regional, intermediate, and  
48 local scales suggest that the geologic framework within an area of paleo-channels exhibits a first-  
49 order control on dune height. The exchange of sediment amongst nearshore, beach and dune in  
50 areas outside this region are scale-independent, implying that barrier islands like PAIS exhibit a  
51 combination of free and forced behaviors that affect the response of the island to sea level rise.

52  
53  
54  
55  
56  
57  
58  
59  
60  
61  
62



## 63 **1 Introduction**

64 Barrier island transgression in response to storms and sea level rise depends to varying degrees on  
65 pre-existing geologic features. The traditional assumption of uniform sand at depth and alongshore  
66 cannot explain many of observations (e.g., Belknap and Kraft, 1985; Houser, 2012; Lentz and  
67 Hapke, 2011; McNinch, 2004; Riggs et al., 1995). Models of barrier island evolution are required to  
68 ascertain the degree to which the island is either *free* (such as a large sand body) or *forced* (i.e.  
69 constrained) by the underlying geology. In a free system, small-scale undulations in the dune line  
70 reinforce natural random processes that occur within the beach-dune system and are not influenced  
71 by the underlying geologic structure. In a forced system, the underlying geologic structure establishes  
72 boundary constraints that control how the island evolves over time. Spatial variation in the dune line  
73 impacts the overall transgression of the island with sea-level rise. Transgression is accomplished  
74 largely through the transport and deposition of beach and dune sediments to the backbarrier as  
75 washover deposits during storms (Houser, 2012; Morton and Sallenger Jr., 2003; Stone et al.,  
76 2004).

77

### 78 1.1 Framework geology controls on barrier island evolution

79 The dynamic geomorphology of a barrier island system is the result of a lengthy, complex and  
80 ongoing history that is characterized by sea level changes and episodes of deposition and erosion  
81 (e.g., Anderson et al., 2015; Belknap and Kraft, 1985; Rodriguez et al., 2001). Previous studies  
82 demonstrate that the underlying geological structure, otherwise termed *framework geology*, of barrier  
83 islands plays a considerable role in the evolution of these coastal landscapes (Belknap and Kraft,  
84 1985; Evans et al., 1985; Kraft et al., 1982; Riggs et al., 1995). For example, antecedent structures  
85 such as paleo-channels, ravinement surfaces, offshore ridge and swale bathymetry, and relict  
86 transgressive features (e.g., overwash deposits) have been suggested to influence barrier island  
87 geomorphology over a wide range of spatial scales (Hapke et al., 2010; Hapke et al., 2016; Houser,  
88 2012; Lentz and Hapke, 2011; McNinch, 2004). In this study, the term “framework geology” is  
89 specifically defined as the topographic surface of incised valleys, paleo-channels, and/or the depth to  
90 ravinement surface beneath the modern beach.

91 As noted by Hapke et al. (2013), the framework geology at the **regional scale** (> 30 km)  
92 influences the geomorphology of an entire island. Of particular importance are the location and size



93 of glacial, fluvial, tidal, and/or inlet paleo-valleys and channels (Belknap and Kraft, 1985; Colman et  
94 al., 1990; Demarest and Leatherman, 1985), and paleo-deltaic systems offshore or beneath the  
95 modern barrier system (Coleman and Gagliano, 1964; Frazier, 1967; Miselis et al., 2014; Otvos and  
96 Giardino, 2004; Twichell et al., 2013). At the regional scale, nonlinear hydrodynamic interactions  
97 between incident wave energy and nearshore ridge and swale bathymetric features can generate  
98 periodic alongshore variations in beach-dune morphology (e.g., Houser, 2012; McNinch, 2004)  
99 that are superimposed on larger-scale topographic variations as a result of transport gradients  
100 (Tebbens, et al., 2002). At the **intermediate scale** (10 - 30 km), feedbacks between geologic  
101 features and relict sediments of the former littoral system (e.g., Honeycutt and Krantz, 2003;  
102 Riggs et al., 1995; Rodriguez et al., 2001; Schwab et al., 2000) act as an important control on  
103 dune formation (Houser et al., 2008) and offshore bathymetric features (e.g., Browder &  
104 McNinch, 2006; Schwab et al., 2013). Framework geology at the **local scale** ( $\leq 10$  km), induces  
105 meso ( $\sim 10^1 - 10^2$  m) to micro-scale ( $< 1$  m) sedimentological changes (e.g., Murray and Thielert,  
106 2004; Schupp, et al., 2006), variations in the thickness of shoreface sediments (Brown and  
107 Macon, 1977; Miselis and McNinch, 2006), and spatial variations in sediment transport across  
108 the island (Houser and Mathew, 2011; Houser, 2012; Lentz and Hapke, 2011).

109 To date, most of what is known regarding barrier island framework geology is based on  
110 studies done at either intermediate or local scales (e.g., Hapke et al., 2010; Lentz and Hapke, 2011;  
111 McNinch, 2004) whereas few studies exist at the regional scale for United States coastlines (Hapke et  
112 al., 2013). The current study focuses on barrier islands in the US and we do not consider work on  
113 barrier islands in other regions. Assessments of framework geology at regional and intermediate  
114 spatial scales for natural and anthropogenically-modified barrier islands are essential for improved  
115 coastal management strategies and risk evaluation since these require a good understanding of the  
116 connections between subsurface geology and surface morphology. For example, studies by Lentz and  
117 Hapke (2011); Lentz et al., (2013) at Fire Island, New York suggest that the short-term  
118 effectiveness of engineered structures is likely influenced by the framework geology. Extending  
119 their work, Hapke et al. (2016) identified distinct patterns of shoreline change that represent  
120 different responses alongshore to oceanographic and geologic forcing. These authors applied  
121 empirical orthogonal function (EOF) analysis to a time series of shoreline positions to better  
122 understand the complex multi-scale relationships between framework geology and contemporary



123 morphodynamics. Gutierrez et al. (2015) used a Bayesian network to predict barrier island  
124 geomorphic characteristics and argue that statistical models are useful for refining predictions of  
125 locations where particular hazards may exist. These examples demonstrate the benefit of using  
126 statistical models as quantitative tools for interpreting coastal processes at multiple spatial and  
127 temporal scales (Hapke et al., 2016).

128

### 129 1.2 Statistical measures of coastline geomorphology

130 It has long been known that many aspects of landscapes exhibit similar statistical properties  
131 regardless of the length or time scale over which observations are sampled (Burrough, 1981). An  
132 often-cited example is the length  $L$  of a rugged coastline (Mandelbrot, 1967), which increases  
133 without bound as the length  $G$  of the ruler used to measure it decreases, in rough accord with the  
134 formula  $L(G) \sim G^{1-D}$ , where  $D \geq 1$  is termed the fractal dimension of the coastline. Andrieu  
135 (1996), however, has identified limitations of the self-similar coastline concept, suggesting that a  
136 coastline may contain irregularities that are concentrated at certain characteristic length-scales  
137 owing to local processes or structural controls. Recent evidence from South Padre Island, Texas  
138 (Houser and Mathew, 2011), Fire Island, New York (Hapke et al., 2010), and Santa Rosa Island,  
139 Florida (Houser et al., 2008) suggests that the geomorphology of barrier islands is affected to  
140 varying degrees by the underlying framework geology and that this geology varies, often with  
141 periodicities, over multiple length-scales. The self-similarity of the framework geology and its  
142 impact on the geomorphology of these barrier islands was not examined explicitly.

143 Many lines of evidence suggest that geological formations in general are inherently rough  
144 (i.e., heterogeneous) and contain multi-scale structure (Bailey and Smith, 2005; Everett and  
145 Weiss, 2002; Radliński et al., 1999; Schlager, 2004). Some of the underlying geological factors  
146 that lead to self-similar terrain variations are reviewed by Xu et al. (1993). In essence, competing  
147 and complex morphodynamic processes, influenced by the underlying geological structure,  
148 operate over different spatiotemporal scales, such that the actual terrain is the result of a complex  
149 superposition of the various effects of these processes (see Lazarus et al., 2011). Although no  
150 landscape is strictly self-similar on all scales, Xu et al. (1993) show that the fractal dimension, as  
151 a global morphometric measure, captures multi-scale aspects of surface roughness that are not



152 evident in conventional local morphometric measures such as slope gradient and profile  
153 curvature.

154         With respect to coastal landscapes, it has been suggested that barrier shorelines are scale  
155 independent, such that the wavenumber spectrum of shoreline variation can be approximated by  
156 a power law at alongshore scales from tens of meters to several kilometers (Lazarus et al., 2011;  
157 Tebbens et al., 2002). However, recent findings by Houser et al. (2015) suggest that the beach-  
158 dune morphology of barrier islands in Florida and Texas is scale-dependent and that  
159 morphodynamic processes operating at swash (0-50 m) and surf-zone (< 1000 m) scales are  
160 different than the processes operating at larger scales. In this context, scale-dependence implies  
161 that a certain number of different processes are simultaneously operative, each process acting at  
162 its own scale of influence, and it is the superposition of the effects of these multiple processes  
163 that shapes the overall behavior and shoreline morphology. This means that shorelines may have  
164 different patterns of irregularity alongshore with respect to barrier island geomorphology, which  
165 has important implications for analyzing long-term shoreline retreat and island transgression.  
166 Lazarus et al. (2011) point out that deviations from power law scaling at larger spatial scales  
167 (tens of km) emphasizes the need for more studies that investigate large-scale shoreline change.  
168 While coastal terrains might not satisfy the strict definition of self-similarity, it is reasonable to  
169 expect them to exhibit long-range dependence (LRD). LRD pertains to signals in which the  
170 correlation between observations decays like a power law with separation, i.e. much slower than  
171 one would expect from independent observations or those that can be explained by a short-  
172 memory process, such as an autoregressive-moving-average (ARMA) with small ( $p, q$ ) (Beran,  
173 1994; Doukhan et al., 2003).

174

### 175 1.3 Research objectives

176 This study performed at Padre Island National Seashore (PAIS), Texas, USA utilizes  
177 electromagnetic induction (EMI) apparent conductivity  $\sigma_a$  responses to provide insight into the  
178 relation between spatial variations in framework geology and surface morphology. Two  
179 alongshore EMI surveys at different spatial scales (100 km and 10 km) were conducted to test  
180 the hypothesis that, like barrier island morphology, subsurface framework geology exhibits LRD.  
181 The  $\sigma_a$  responses, which are sensitive to parameters such as porosity and mineral content, are



182 regarded herein as a rough proxy for subsurface framework geology (Weymer et al., 2015). This  
183 assumes, of course, that alongshore variations in salinity and water saturation, and other factors  
184 that shape the  $\sigma_a$  response, can be neglected to first order. A corroborating 800 m ground-  
185 penetrating radar (GPR) survey, providing an important check on the variability observed within  
186 the EMI signal, confirms the location of a previously identified paleo-channel (Fisk, 1959) at  $\sim 5$   
187 – 10 m depth. The overall geophysical survey design allows for a detailed evaluation of the long-  
188 range-dependent structure of the framework geology over a range of length scales spanning  
189 several orders of magnitude. We explore the applicability of autoregressive integrated moving-  
190 average (ARIMA) processes as statistical models that describe EMI and Light Detection and  
191 Ranging (LiDAR) spatial data series. This paper introduces the use of a generalized fractional  
192 ARIMA (0, $d$ ,0) process (Hosking, 1981) that is specifically designed to model LRD for a given  
193 data series using a single differencing non-integer parameter  $d$ . The parameter  $d$  can be used in  
194 the present context to discriminate between *forced*, scale-dependent controls by the framework  
195 geology; i.e., stronger LRD ( $d \rightarrow 0.5$ ) and *free* behavior that is scale-independent; i.e., weaker  
196 LRD ( $0 \leftarrow d$ ). In other words, it is the particular statistical characteristics of the framework  
197 geology LRD at PAIS that we are trying to ascertain from the EMI  $\sigma_a$  signal, with the suggestion  
198 that  $\sigma_a$  measurements can be used similarly at other sites to reveal the hidden LRD characteristics  
199 of the framework geology.

200

## 201 **2 Background and regional setting**

### 202 2.1 Utility of electromagnetic methods in coastal environments

203 Methods to ascertain the alongshore variability of framework geology, and to test long-range  
204 dependence, are difficult to implement and can be costly. Cores provide detailed point-wise  
205 geologic data; however, they do not provide laterally continuous subsurface information (Jol et  
206 al., 1996). Alternatively, geophysical techniques including seismic and GPR provide spatially  
207 continuous stratigraphic information (e.g., Buynevich et al., 2004; Neal, 2004; Nummedal and  
208 Swift, 1987; Tamura, 2012), but they are not ideally suited for LRD testing because the data  
209 combine depth and lateral information at a single acquisition point. Moreover, GPR signals  
210 attenuate rapidly in saltwater environments whereas seismic methods are labor-intensive and  
211 cumbersome. On the other hand, terrain conductivity profiling is an easy-to-use alternative that



212 has been used in coastal environments to investigate fundamental questions involving;  
213 instrument performance characteristics (Delefortrie et al., 2014; Weymer et al., 2016),  
214 groundwater dynamics (Stewart, 1982; Fitterman and Stewart, 1986; Nobes, 1996; Swarzenski,  
215 and Izbicki, 2009), and framework geology (Seijmonsbergen et al. 2004; Weymer et al. 2015).  
216 Previous studies combining EMI with either GPR (Evans and Lizarralde, 2011) or coring  
217 (Seijmonsbergen et al. 2004) demonstrate the validity of EM measurements as a means to  
218 quantify alongshore variations in the framework geology of coastlines.

219 In the alongshore direction, Seijmonsbergen et al. (2004) used a Geonics EM34™ terrain  
220 conductivity meter oriented in the horizontal dipole mode with intercoil separation and station  
221 spacing both of 20 m. This configuration provides an exploration depth of roughly 15 m. A 14.5  
222 km-length EMI transect was collected along the backbeach crossing a former outlet of the Rhine  
223 River, Netherlands to evaluate alongshore variations in subsurface lithology. The survey was  
224 conducted in an area that was previously characterized by drilling and these data were used to  
225 calibrate the  $\sigma_a$  measurements. The results from the study suggest that coastal sediments can be  
226 classified according to  $\sigma_a$  signature. The range of  $\sigma_a$  values was categorized into three groups. The  
227 first group of low  $\sigma_a$  20 – 45 millisiemens per meter (mS/m) with low-variability amplitudes was  
228 interpreted as beach sands. The second group of medium  $\sigma_a$  values (20 – 90 mS/m) with large  
229 variability corresponded to clay and peat layers of varying thickness. A third group of high  $\sigma_a$  values  
230 (60 – 190 mS/m) with large variability was interpreted as clay-rich brackish channel deposits. The  
231 authors suggest that high  $\sigma_a$  values occur in areas where the underlying conductive layer is thick and  
232 close to the surface. Although Seijmonsbergen et al. (2004) suggest that EMI surveys are a rapid,  
233 inexpensive method to investigate subsurface lithology they also acknowledge that variations in  
234 salinity as a result of changing hydrologic conditions, storm activity and/or tidal influence confound  
235 the geological interpretation and should be investigated in further detail (see Weymer et al., 2016).

236 The challenge on many barrier islands and protected National Seashores is obtaining  
237 permission for extracting drill cores to validate geophysical surveys. At PAIS, numerous areas  
238 along the island are protected nesting sites for the endangered Kemp's ridley sea turtle,  
239 migratory birds, while other areas comprise historic archeological sites with restricted access.  
240 Thus, coring is not allowed and only non-invasive techniques, such as EMI/GPR are permitted.  
241



## 242 2.2 Regional setting

243 North Padre Island is part of a large arcuate barrier island system located along the Texas Gulf of  
244 Mexico coastline and is the longest undeveloped barrier island in the world. The island is one of  
245 ten national seashores in the United States and is protected and managed by the National Park  
246 Service, a bureau of the Department of the Interior. PAIS is 129 km in length, and is an ideal  
247 setting for performing EMI surveys because there is minimal cultural noise to interfere with the  
248  $\sigma_a$  signal, which as stated earlier we regard as a proxy for alongshore variations in framework  
249 geology (Fig. 1). Additionally, the island is well-covered by high-resolution aerial LiDAR data.  
250 The island is not dissected by inlets or navigation channels (excluding Mansfield Channel  
251 separating north and south Padre Island), or modified by engineered structures (e.g., groynes,  
252 jetties, etc.) that often interfere with natural morphodynamic processes (see Talley et al., 2003).  
253 The above characteristics make the study area an exceptional location for investigating the  
254 relationships between large-scale framework geology and surface morphology.

255       Relatively little is known about the framework geology at PAIS, especially its alongshore  
256 variability. A notable exception is the information obtained from a series of coring and seismic  
257 surveys conducted by Fisk (1959) in the central region of Padre Island ( $\sim 27^\circ$  N). As described in  
258 Weymer et al. (2015a; Fig. 3), locations of paleo-channels were established by Fisk (1959) based  
259 on 3,000 cores and several seismic surveys. More than 100 borings were drilled to the top of the  
260 late Pleistocene surface (tens of m depth) providing sedimentological data for interpreting the  
261 depth and extent of the various paleo-channels. These cores were extracted  $\sim 60$  years ago, but  
262 the remnant Pleistocene and Holocene fluvial/deltaic features described in Fisk's study likely  
263 have not changed over decadal time scales.

264       Geologic interpretations based on the Fisk (1959) data suggest that the thickness of the  
265 modern beach sands is  $\sim 2 - 3$  m, and they are underlain by Holocene shoreface sands and muds  
266 to a depth of  $\sim 10 - 15$  m (Brown and Macon, 1977; Fisk, 1959). The Holocene deposits lie upon  
267 a Pleistocene ravinement surface of fluvial-deltaic sands and muds and relict transgressive  
268 features. A network of buried valleys and paleo-channels in the central segment of the island, as  
269 interpreted by Fisk (1959), exhibits a dendritic, tributary pattern. The depths of the buried valleys  
270 inferred from seismic surveys range from  $\sim 25 - 40$  m (Brown and Macon, 1977). These  
271 channels have been suggested to incise into the Pleistocene paleo-surface and became infilled



272 with sands from relict Pleistocene dunes and fluvial sediments reworked by alongshore currents  
273 during the Holocene transgression (Weise and White, 1980). However, the location and cross-  
274 sectional area of each valley and paleo-channel alongshore is not well-constrained. It is also  
275 possible that other channels exist other than those identified by Fisk (1959).

276 As presented in Weymer et al. (2015a), minima in the alongshore  $\sigma_a$  signal are spatially  
277 correlated with the locations of these previously identified geologic features. This observation  
278 provides an impetus for using EMI to map the known, and any previously unidentified, geologic  
279 features alongshore. The observed beach-dune morphology and other metrics such as island  
280 width are highly variable and controlled to an unknown extent by the framework geology both  
281 within and outside the known paleo-channel regions. The fact that much of the framework  
282 geology at PAIS is poorly known provides additional motivation for integrating subsurface  
283 geophysical methods and surface observations to analyze, from a statistical standpoint, the key  
284 geologic controls on island morphology within the study area.

285

### 286 **3 Methods**

287 A combination of geophysical, geomorphological, and statistical methods are used in this study  
288 to quantify the relationships between framework geology and surface geomorphology at PAIS. A  
289 description of the EMI, GPR, geomorphometry and statistical techniques is provided in the  
290 following sections.

291

#### 292 **3.1 Field EMI and GPR surveys**

293 Profiles of EMI  $\sigma_a$  responses typically are irregular and each datum represents a spatial averaging  
294 of the bulk subsurface electrical conductivity  $\sigma$ , which in turn is a function of a number of  
295 physical properties (e.g., lithology, porosity, water content, salinity, etc.). The “sensor footprint”,  
296 or subsurface volume over which the spatial averaging is performed, is dependent on the  
297 separation between the TX – RX coils (1.21 m in this study), and the transmitter frequency. The  
298 horizontal extent, or radius, of the footprint can be more or less than the step-size between  
299 subsequent measurements along the profile. The sensor footprint determines the volume of  
300 ground that contributes to  $\sigma_a$  at each acquisition point, and as will be discussed later, the radius  
301 of the footprint has important implications for analyzing LRD. The footprint radius depends on



302 frequency and ground conductivity, but is likely to be of the same order as, but slightly larger  
303 than, the intercoil spacing. Two different station-spacings were used to examine the correlation  
304 structure of  $\sigma_a$  as a function of spatial scale. An island-scale alongshore survey of  $\sim 100$  km  
305 length was performed using a 10 m station spacing (station spacing  $\gg$  footprint radius) such that  
306 each  $\sigma_a$  measurement was recorded over an independently sampled volume of ground.  
307 Additionally, a sequence of  $\sigma_a$  readings was collected at 1 m spacing (station spacing  $<$  footprint  
308 radius) over a profile length of 10 km within the Fisk (1959) paleo-channel region of the island.  
309 This survey design allows for comparison of the long-range-dependent structure of the  
310 framework geology over several orders of magnitude ( $10^0 - 10^5$  m).

311 The 100-km-long alongshore EMI survey was performed during a series of three field  
312 campaigns, resulting in a total of 21 (each of length  $\sim 4.5$  km) segments that were collected  
313 during October 9 – 12<sup>th</sup>, 2014, November 15 – 16<sup>th</sup>, 2014, and March 28<sup>th</sup>, 2015. The EMI  $\sigma_a$   
314 responses were stitched together by importing GPS coordinates from each measurement into  
315 ArcGIS<sup>TM</sup> to create a single composite spatial data series. The positional accuracy recorded by a  
316 TDS Recon PDA equipped with a Holux<sup>TM</sup> WAAS GPS module was found to be accurate within  
317  $\sim 1.5$  m. An additional 10 km survey was performed along a segment of the same 100 km survey  
318 line in one day on March 29<sup>th</sup>, 2015, to determine whether varying hydrologic conditions in both  
319 space and time, which are discussed below, play a deleterious role in resolving the framework  
320 geology. This second composite data series consists of 8 stitched segments.

321 The same multi-frequency GSSI Profiler EMP-400<sup>TM</sup> instrument was used for each  
322 segment. All transects were located in the backbeach environment  $\sim 25$  m inland from the mean  
323 tide level (MTL). This location was chosen to reduce the effect of changing groundwater  
324 conditions in response to nonlinear tidal forcing, which may be significant closer to the  
325 shoreline. The sensor has reduced ability to detect lateral changes in the underlying geology  
326 during wet conditions such as during or immediately after significant rainfall events, or at high  
327 tide near the shoreline, since electrical conductivity increases rapidly with water content. The  
328 transect locations also avoid the large topographic variations (see Santos et al., 2009) fronting the  
329 foredune ridge that can reduce the efficiency of data acquisition and influence the EMI signal. In  
330 a companion study, Weymer et al. (2016) demonstrated that the  $\sigma_a$  signal at the beachfront exhibits  
331 a step-like response over the course of a tidal cycle; however, this effect is less pronounced



332 further inland where the surveys in the present study were collected. Their study shows that the  
333 difference between high-tide and low-tide EMI  $\sigma_a$  measurements is as large as 50 mS/m at the  
334 backbeach, but this difference is less than 9% of the range of  $\sigma_a$  variations observed ( $\sim 50 - 600$   
335 mS/m) along the entire length of the island. As will be shown later, there is not a direct  
336 correlation between high tide and high  $\sigma_a$  values. Thus, we assume the tidal influence on the EMI  
337 signal can be neglected over the spatial scales of interest in the present study. Nevertheless, the  
338 duration and approximate tidal states of each survey was documented in order to compare with  
339 the EMI signal (see Weymer et al., 2016). Tidal data were accessed from NOAA's Tides and  
340 Currents database (NOAA, 2015b). Padre Island is microtidal and the mean tidal range within the  
341 study area is 0.38 m (NOAA, 2015a). A tidal signature in EMI signals may become more significant  
342 at other barrier islands with larger tidal ranges.

343 For all surveys, the EMI profiler was used in a vertical dipole orientation with TX and  
344 RX coils aligned in the (P-mode) direction parallel to the profile line (Weymer et al., 2016).  
345 Measurements were made at a constant step-size to simplify the data analysis; for example,  
346 ARIMA models require that data are taken at equal intervals (see Cimino et al., 1999). The EMI  
347 profiler was carried at a height of 0.7 m above the ground to mitigate noise from the mainly non-  
348 metallic debris on the beach that unfortunately is scattered along the island (Weymer et al.,  
349 2016). Although the sensor is capable of recording three frequencies simultaneously (see GSSI,  
350 2007), we choose herein to focus on data collected at 3 kHz, resulting in a depth of investigation  
351 (DOI) of  $\sim 3.5 - 6.4$  m over the range of conductivities found within the study area (Weymer et  
352 al., 2016; Table 1.). Because the depth of the modern beach sands is  $\sim 2 - 3$  m or greater (see  
353 Brown and Macon, 1977; page 56, Figure 15), variations in the depth to shoreface sands and  
354 muds is assumed to be within the DOI of the profiler, which may not be captured at the higher  
355 frequencies also recorded by the sensor (i.e., 10, and 15 kHz).

356 An 800 m GPR survey was performed on August 12<sup>th</sup>, 2015 across one of the paleo-  
357 channels previously identified Fisk (1959) located within the 10 km EMI survey for comparison  
358 with the  $\sigma_a$  measurements. We used a Sensors and Software PulseEKKO Pro<sup>®</sup> system for this  
359 purpose. A survey grade GPS with a positional accuracy of 10 cm was used to match the  
360 locations and measurements between the EMI/GPR surveys. Data were acquired in reflection  
361 mode at a nominal frequency of 100 MHz with a standard antenna separation of 1 m and a step-



362 size of 0.5 m. The instrument settings resulted in a DOI of up to 15 m. Minimal processing was  
363 applied to the data and includes a dewow filter and migration (0.08 m/ns), followed by AGC gain  
364 (see Neal, 2004). Given The theory and operational principles of GPR are discussed in many  
365 places (e.g. Everett, 2013; Jol, 2008) and will not be reviewed here.

366

### 367 3.2 Geomorphometry

368 Topographic information was extracted from aerial LiDAR data that were collected by the Army  
369 Corps of Engineers (USACE) in 2009 as part of the West Texas Aerial Survey project to assess  
370 post-hurricane conditions of the beaches and barrier islands along the Texas coastline. This  
371 dataset is the most recent publicly available LiDAR survey of PAIS and it provides essentially  
372 complete coverage of the island. With the exception of Hurricane Harvey, which made landfall  
373 near Rockport, Texas as a Category 4 storm in late August, 2017, Padre Island has not been  
374 impacted by a hurricane since July 2008, when Hurricane Dolly struck South Padre Island as a  
375 Category 1 storm (NOAA, 2015a). The timing of the LiDAR and EMI surveys in this study  
376 precede the impacts of Hurricane Harvey, and it is assumed that the surface morphology across  
377 the island at the spatial scales of interest (i.e.,  $10^1 - 10^2$  km) did not change appreciably between  
378 2009 and 2015.

379 A 1-m resolution DEM was created from 2009 LiDAR point clouds available from  
380 NOAA's Digital Coast (NOAA, 2017). The raw point cloud tiles were merged to produce a  
381 combined point cloud of the island within the PAIS National Seashore. The point clouds were  
382 processed into a continuous DEM using the ordinary kriging algorithm in SAGA GIS, which is  
383 freely available open-source software ([www.saga-gis.org/](http://www.saga-gis.org/)); and subsequent terrain analysis was  
384 conducted using an automated approach involving the relative-relief metric (Wernette et al.,  
385 2016). Relative relief is a measure of topographic position of the center pixel compared to the  
386 minimum and maximum pixel elevations within a given computational window. Several other  
387 morphometrics including beach width, dune height, and island width were extracted from the  
388 DEM using a recently developed automated multi-scale approach (see Wernette et al., 2016).  
389 This technique extracts the open-water shoreline (in this case the Gulf of Mexico shoreline) and  
390 backbarrier shoreline based on elevation thresholds and uses them to calculate beach and island  
391 width referenced to mean sea-level (MSL). Dune metrics including dune crest, dune heel, and



392 dune toe elevations are calculated based on the average relative relief (RR) to determine where  
393 the dune begins, crests, and ends along every shore-normal profile in a DEM. This process is  
394 repeated for all such profiles at a 1 m spacing along the entire length of PAIS to generate a  
395 continuous dataset of alongshore dune height and volume. A detailed description of the  
396 procedure for extracting each metric is provided in Wernette et al. (2016).

397 Each morphometric feature was extracted by averaging the RR values across window  
398 sizes of 21 m x 21 m, 23 m x 23 m, and 25 m x 25 m. The choice of window size is based on  
399 tacit *a priori* knowledge and observations of the geomorphology in the study area. Larger  
400 window sizes will better capture smoother beach and dune features by reducing sensitivity to the  
401 fine-scale variability induced by measurement error inherent in LiDAR-derived DEMs, as well  
402 as natural terrain irregularities (Wernette et al., 2016). Each DEM series is paired with the  $\sigma_a$   
403 profile by matching the GPS coordinates (latitude and longitude) recorded in the field by the  
404 EMI sensor. Cross-sectional DEM profiles oriented perpendicular to the shoreline were analyzed  
405 every 10 m (y-coordinate) along the EMI profile to match the same 10 m sampling interval of the  
406  $\sigma_a$  measurements. The terrain variations along each cross-shore profile are summed to calculate  
407 beach and island volume based on the elevation thresholds mentioned above. Dune volume is  
408 calculated by summing the pixel elevations starting at the dune toe, traversing the dune crest, and  
409 ending at the dune heel. In total, six DEM morphometrics were extracted as spatial data series to  
410 be paired with the EMI data, each having an identical sample size ( $n = 9,694$ ), which is  
411 sufficiently large for statistical ARIMA modeling.

412

### 413 3.3 Statistical methods

414 Although the procedures for generating the EMI and LiDAR datasets used in this study  
415 are different, the intended goal is the same; to produce spatial data series that contain similar  
416 numbers of observations for comparative analysis using a combination of signal processing and  
417 statistical modeling techniques. The resulting signals comprising each data series represent the  
418 spatial averaging of a geophysical (EMI) or geomorphological (DEM) variable that contains  
419 information about the important processes-form relationships between subsurface geologic  
420 features and island geomorphology that can be teased out by means of comparative analysis  
421 (Weymer et al., 2015a). Because we are interested in evaluating these connections at both small



422 and large spatial scales, our first approach is to determine the autocorrelation function and Hurst  
423 coefficient (self-similarity parameter)  $H$  and hence verify whether the data series are  
424 characterized by short and/or long-range memory (Beran, 1992; Taquu et al., 1995). LRD occurs  
425 when the autocorrelation within a series, at large lags, tend to zero like a power function, and so  
426 slowly that the sums diverge (Doukhan et al., 2003). LRD is often observed in natural time series  
427 and is closely related to self-similarity, which is a special type of LRD.

428 The degree of LRD is related to the scaling exponent,  $H$  of a self-similar process, where  
429 increasing  $H$  in the range  $0.5 < H \leq 1.0$  indicates an increasing tendency towards such an effect  
430 (Taquu, 2003). Large correlations at small lags can easily be detected by models with short-  
431 memory (e.g., ARMA, Markov processes) (Beran, 1994). Conversely, when correlations at large  
432 lags slowly tend to zero like a power function, the data contain long-memory effects and either  
433 fractional Gaussian noise (fGn), or ARIMA models may be suitable (Taquu et al., 1995). The  
434 R/S statistic is the quotient of the range of values in a data series and the standard deviation  
435 (Beran, 1992, 1994; Hurst, 1951; Mandelbrot and Taquu, 1979). When plotted on a log/log plot,  
436 the resulting slope of the best-fit line gives an estimate of  $H$ , which is useful as a diagnostic tool  
437 for estimating the degree of LRD (see Beran, 1994). For a given number of observations  $X_1, X_2,$   
438  $\dots, X_n$ , a partial sum sequence is defined by  $S_m = X_1 + \dots + X_m$ , for  $m = 0, 1, \dots$  and  $m < n$  (with  $S_0$   
439  $= 0$ ). The R/S statistic is then calculated by (see Samorodnitsky, 2007):

$$440 \quad \frac{R}{S}(X_1, \dots, X_n) = \frac{\max_{0 \leq i \leq n} (S_i - \frac{i}{n} S_n) - \min_{0 \leq i \leq n} (S_i - \frac{i}{n} S_n)}{\sqrt{\left(\frac{1}{n} \sum_{i=1}^n (x_i - \frac{1}{n} S_n)^2\right)}} \quad (1)$$

441 where,  $S_n/n$  is the mean of the sample. It has been suggested that R/S tends to give biased  
442 estimates of  $H$ , too low for  $H > 0.72$  and too high for  $H < 0.72$  (Bassingthwaigthe and Raymond,  
443 1994), which was later confirmed by Malamud and Turcotte (1999). Empirical trend corrections  
444 to the estimates of  $H$  can be made by graphical interpolation, but are not applied here because of  
445 how the regression is done. The R/S analysis in this study was performed using signal analysis  
446 software AutoSignal™ to identify whether a given signal is distinguishable from a random,  
447 white noise process and, if so, whether the given signal contains LRD. The  $H$  value is calculated  
448 by an inverse variance-weighted linear least-squares curve fit using the logarithms of the R/S and



449 the number of observations, which provides greater accuracy than other programs that compute  
450 the Hurst coefficient.

451 Two of the simplest statistical time series models that can account for LRD are fGn and  
452 ARIMA. In the former case, fGn and its “parent” fBm are used to evaluate stationary and  
453 nonstationary fractal signals, respectively (see Eke et al., 2000; Everett and Weiss, 2002). Both  
454 fGn and fBm are governed by two parameters: variance  $\sigma^2$ ; and the scaling parameter,  $H$  (Eke et  
455 al., 2000). A more comprehensive class of time series models that has similar capability to detect  
456 long-range structure is ARIMA. Because fGn and fBm models have only two parameters, it is  
457 not possible to model the short-range components. Additional parameters in ARIMA models are  
458 designed to handle the short-range component of the signal, as discussed by Taqqu et al. (1995)  
459 and others. Because the EMI data series presumably contain both short-range and long-range  
460 effects, we chose to use ARIMA as the analyzing technique.

461 ARIMA models are used across a wide range of disciplines and have broad applicability  
462 for understanding the statistical structure of a given data series as it is related to some physical  
463 phenomenon (see Beran, 1992, 1994; Box and Jenkins, 1970; Cimino et al., 1999; Granger and  
464 Joyeux, 1980; Hosking, 1981; Taqqu et al., 1995). The statistical ARIMA model of a given data  
465 series is defined by three terms ( $p,d,q$ ), where  $p$  and  $q$  indicate the order of the autoregressive  
466 (AR) and moving average (MA) components, respectively and  $d$  represents a differencing, or  
467 integration term (I) that is related to LRD. The AR element,  $p$ , represents the effects of adjacent  
468 observations and the MA element,  $q$ , represents the effects on the process of nearby random  
469 shocks (Cimino et al., 1999; De Jong and Penzer, 1998). However, in the present study our series  
470 are reversible spatial series that can be generated, and are identical, with either forward or  
471 backward acquisition, unlike a time series. Both  $p$  and  $q$  parameters are restricted to integer  
472 values (e.g., 0, 1, 2), whereas the integration parameter,  $d$ , represents potentially long-range  
473 structure in the data. The differencing term  $d$  is normally evaluated before  $p$  and  $q$  to identify  
474 whether the process is stationary (i.e., constant mean and  $\sigma^2$ ). If the series is nonstationary, it is  
475 differenced to remove either linear ( $d = 1$ ) or quadratic ( $d = 2$ ) trends, thereby making the mean  
476 of the series stationary and invertible (Cimino et al., 1999), thus allowing determination of the  
477 ARMA  $p$  and  $q$  parameters.



478 Here, we adopt the definitions of an ARMA ( $p,q$ ), and ARIMA ( $p,d,q$ ) process following  
479 the work of Beran (1994). Let  $p$  and  $q$  be integers, where the corresponding polynomials are  
480 defined as:

$$481 \quad \phi(x) = 1 - \sum_{j=1}^p \phi_j x^j, \tag{2}$$

$$483 \quad \psi(x) = 1 + \sum_{j=1}^q \psi_j x^j.$$

484  
485 It is important to note that all solutions of  $\phi(x_0) = 0$ , and  $\psi(x) = 0$  are assumed to lie outside  
486 the unit circle. Additionally, let  $\epsilon_t (t = 1, 2, \dots)$  be independent, and identically distributed  
487 normal variables with zero variance  $\sigma_\epsilon^2$  such that an ARMA ( $p,q$ ) process is defined by the  
488 stationary solution of:

$$490 \quad \phi(B)X_t = \psi(B)\epsilon_t \tag{3}$$

491  
492 where,  $B$  is the backward shift operator  $BX_t = X_{t-1}, B^2X_t = X_{t-2}, \dots$  and, specifically, the  
493 differences can be expressed in terms of  $B$  as;  $X_t - X_{t-1} = (1 - B)X_t, (X_t - X_{t-1}) - (X_{t-1} -$   
494  $X_{t-2}) = (1 - B)^2X_t \dots$  Alternatively, an ARIMA ( $p,d,q$ ) process  $X_t$  is formally defined as:

$$496 \quad \phi(B)(1 - B)^d X_t = \psi(B)\epsilon_t \tag{4}$$

497  
498 where, equation (3) holds for a  $d$ th difference  $(1 - B)^d X_t$ .

499 As mentioned previously, a more general form of ARIMA ( $p,d,q$ ) is the fractional  
500 ARIMA process, or FARIMA, where the differencing term  $d$  is allowed to take on fractional  
501 values. If  $d$  is a non-integer value for some  $-0.5 < d < 0.5$  and  $\{x_t\}$  is a stationary process as  
502 indicated by equation 4, then the model by definition is called a FARIMA process where  $d$ -  
503 values in the range  $0 < d < 0.5$  of are of particular interest herein because geophysically-relevant  
504 LRD occurs for  $0 < d < 0.5$ , whereas  $d > 0.5$  means that the process is nonstationary, but  
505 nonintegrable (Beran, 1994; Hosking, 1981). A special case of a FARIMA process explored in



506 the current study is ARIMA (0d0), also known as fractionally-differenced white noise (Hosking,  
507 1981), which is defined by Beran (1994) and others as:

508

$$509 \quad X_t = (1 - B)^{-d} \epsilon_t. \quad (5)$$

510

511 For  $0 < d < 0.5$ , the ARIMA (0d0) process is a stationary process with long-range structure and  
512 is useful for modeling LRD. According to Hosking (1981),  $\{x_t\}$  is called an ARIMA (0d0)  
513 process and is of particular interest in modelling LRD as  $d$  approaches 0.5 because in such cases  
514 the correlations and partial correlations of  $\{x_t\}$  are all positive and decay slowly towards zero as  
515 the lag increases, while the spectral density of  $\{x_t\}$  is concentrated at low frequencies. As shown  
516 later, different values of the  $d$  parameter provide further insight into the type of causative  
517 physical processes that generate each data series. When  $d < 0.5$ , the series  $\{x_t\}$  is stationary,  
518 which has an infinite moving average MA representation that highlights long-range trends or  
519 cycles in the data. Conversely, when  $d > -0.5$ , the series  $\{x_t\}$  is invertible and has an infinite  
520 autoregressive AR representation (see Hosking, 1981). When  $-0.5 < d < 0$ , the stationary, and  
521 invertible, ARIMA (0d0) process is dominated by short-range effects and is antipersistent. When  
522  $d = 0$ , the ARIMA (000) process is white noise, having zero correlations and a constant spectral  
523 density.

524 Following the methodology proposed by Box and Jenkins (1970), there are three phases  
525 that characterize ARIMA modeling: *identification*, *estimation*, and *diagnostic testing*. The  
526 primary task of the first phase is to identify the autocorrelation function(s) and any patterns in the  
527 data (e.g., autocorrelation function, R/S analysis), and to manipulate the data (if necessary) to  
528 achieve stationarity before an appropriate model is chosen (Linden et al., 2003). After an  
529 appropriate model is selected (e.g., ARMA, ARIMA, etc.), statistical software is used in the  
530 second phase to generate estimates of each model parameter ( $p, d, q$ ) in order to achieve a good  
531 model fit. Tasks included in the third phase involve examining the residual score, or root-mean-  
532 square error (RMSE), to determine if there are patterns remaining in the data that are not  
533 accounted for. Residual scores, or the mismatch between the values predicted by the model and  
534 the actual values of the data series, should show that there are no significant autocorrelations



535 among the residuals (Linden et al., 2003). The best model fit is determined by the smallest  
536 residual score, which is the sum of the squares of the residuals (i.e., RMSE).

537 Identification of an appropriate model is accomplished by finding small values of  
538 elements  $p, d, q$  (usually between 0 – 2) that accurately fit the most significant patterns in the data  
539 series. When a value of an element is 0, that element is not needed. For example, if  $d = 0$  the  
540 series does not contain a significant long-range component, whereas if  $p = q = 0$ , the model does  
541 not exhibit significant short-range effects. If  $p, d, q \neq 0$ , the model contains a combination of both  
542 short and long-memory effects.

543 Time series modeling is traditionally used for either forecasting future values or assigning  
544 missing values within the data series. In this study, we are interested in determining the orders of  
545  $p, d, q$  not for forecasting or filling in missing data, but rather for gaining physical insight into the  
546 structure of EMI  $\sigma_a$  responses, and since it is a proxy, the structure of the framework geology.  
547 Different combinations of  $(p, d, q)$  provide insights into the degree or strength of LRD within a  
548 data series and, in the present context in which EMI and DEM are jointly analyzed, the best-fit  
549  $(p, d, q)$  values can be used to discern how the various length-scales within the framework  
550 geology and island morphology are related.

551

## 552 **4 Results**

### 553 4.1 Spatial data series

#### 554 4.1.1 EMI and GPR surveys

555 The 100 km EMI survey (Fig. 2a) represents (to our knowledge) the longest continuous ground-  
556 based survey using a terrain conductivity meter ever performed. The unprocessed (raw) EMI  $\sigma_a$   
557 responses show a high degree of variability along the island. To reduce the effect of instrument  
558 drift caused by temperature, battery and other systematic variations through the acquisition  
559 interval, a drift correction was applied to each segment, the segments were then stitched together,  
560 following which a regional linear trend removal was applied to the composite dataset. High-  
561 amplitude responses within the EMI signal generally exhibit a higher degree of variability  
562 (multiplicative noise) compared to the low-amplitude responses. Higher  $\sigma_a$  readings correspond  
563 to a small sensor footprint and have enhanced sensitivity to small-scale near-surface  
564 heterogeneities (see Guillemoteau and Tronicke, 2015). Low  $\sigma_a$  readings suggest the sensor is



565 probing greater depths and averaging over a larger footprint. In that case, the effect of fine-scale  
566 heterogeneities that contribute to signal variability is suppressed.

567 The 10 km alongshore survey is located within an inferred paleo-channel region (Fisk,  
568 1959), providing some *a priori* geologic constraints for understanding the variability within the  
569 EMI signal (Fig. 2b). Here, the sample size is  $n = 10,176$ , permitting a quantitative comparison  
570 with the 100-km-long data series since they contain a similar number of observations. Unlike the  
571 100 km survey, successive footprints of the sensor at each subsequent measurement point  
572 overlap along the 10 km survey. The overlap enables a fine-scale characterization of the  
573 underlying geological structure because the separation between the TX – RX coils (1.21 m), a  
574 good lower-bound approximation of the footprint, is greater than the step-size (1 m).

575 The overall trend in  $\sigma_a$  for the 10 km survey is comparable to that of the 100 km survey,  
576 where regions characterized by high and low amplitude signals correspond to regions of high and  
577 low variability, respectively, implying that multiplicative noise persists independently of station  
578 spacing. The decrease in  $\sigma_a$  that persists between  $\sim 2.5 - 6$  km along the profile (Fig. 2b)  
579 coincides in location with two paleo-channels, whereas a sharp reduction in  $\sigma_a$  is observed at  $\sim$   
580 8.2 km in close proximity to a smaller channel. Most of the known paleo-channels are located  
581 within the 10 km transect and likely contain resistive infill sands that should generate lower and  
582 relatively consistent  $\sigma_a$  readings (Weymer et al., 2015a). The low  $\sigma_a$  signal caused by the sand  
583 indirectly indicates valley incision, since it is diagnostic of a thicker sand section, relatively  
584 unaffected by the underlying conductive layers. Thus, it is reasonable to assume that reduced  
585 variability in the signal is related to the framework geology within the paleo-channels, which we  
586 now compare with a GPR profile.

587 To corroborate the capability of the EMI data to respond to subsurface geology, an 800 m  
588 GPR survey confirms the location of a previously identified paleo-channel (Fisk, 1959) at  $\sim 5 -$   
589 10 m depth (Fig. 3). A continuous undulating reflector from  $\sim 150 - 800$  m along the profile is  
590 interpreted to be the surface mapped by Fisk (1959) who documented a paleo-channel at this  
591 location with a depth of  $\sim 8$  m. Although the paleo-surface is within the detection limits of the  
592 GPR, it is likely that the DOI of the EMI data ( $\sim 3 - 6$  m) is not large enough to probe  
593 continuously along the contact between the more conductive ravinement surface and the less  
594 resistive infill sands. Along the transect at shallower depths highlighted by the red box in the



595 lower radargram (Fig. 3), low EMI  $\sigma_a$  values correspond to fine stratifications in the GPR  
596 section, which is common for beach sands with little clay content that are not saline-saturated.  
597 The EMI highs between  $\sim 450 - 530$  m coincide with parts of the GPR section that do not have  
598 the fine stratification and this may indicate the presence of clay or saline water. Here, the high  
599 conductivity zone for both the GPR and EMI is located within a recovering washover channel  
600 overlying the paleo-channel that is evident in the satellite imagery in the upper-left panel of Fig.  
601 3. The overwash deposits consisting of a mix of sand and finer-grained backbarrier sediments  
602 likely mask the EMI sensors' ability to probe greater depths. Nonetheless, the high conductivity  
603 zone represents a smaller  $\sim 100$  m segment within the  $\sim 500$ -m-wide paleo-channel, suggesting  
604 that variations in the EMI responses outside this zone correspond to variations in the framework  
605 geology imaged by GPR.

606

#### 607 4.1.2 LiDAR-derived DEM morphometrics

608 The LiDAR-derived DEM spatial data series along the 100 km transect are presented in Fig. 4.  
609 Each data series is shown with respect to the areal DEM of the study area where the approximate  
610 locations of each closely-spaced paleo-channel are highlighted in gray. This visualization allows  
611 a qualitative analysis of the spatial relationships between subsurface information encoded in the  
612  $\sigma_a$  signal, and surface morphology over the entire length of the barrier island.

613 The morphology of the beach-dune system, as well as island width, changes substantially  
614 from north to south. In the paleo-channel region, beach width decreases considerably and is more  
615 variable. Beach width generally increases towards the northern section of the island. The volume  
616 of the beach tends to be lowest in the northern zone, varies considerably in the central part of the  
617 island, then stabilizes and gradually decreases towards the south. These zones correspond to the  
618 southern (0 – 30 km), central (30 – 60 km), and northern (60 – 100 km) sections of the island.  
619 Alongshore dune heights are greater in the south, become more variable in the paleo-channel  
620 region, and decrease in the north except for the area adjacent to Baffin Bay. Dune volume is  
621 lowest in the northern section, intermittently increases in the central zone and slightly decreases  
622 towards the south. The island is considerably narrower between Mansfield Channel and Baffin  
623 Bay (see Fig. 2a), increasing in width significantly in the northern zone; island volume follows a  
624 similar trend. Overall,  $\sigma_a$  values are lower northward of the paleo-channel region compared to the



625 southern zone where  $\sigma_a$  increases substantially. However, the lowest  $\sigma_a$  values are located within  
626 the region of paleo-channels inferred by Fisk (1959) supporting previous findings in the study  
627 area by Weymer et al. (2015a) that suggest a potential geologic control on alongshore  
628 geomorphic features.

629 Each spatial data series (Fig. 4a – 4g) represents a different superposition of effects  
630 caused by physical processes operating across a wide range of temporal and length scales  
631 (Weymer et al., 2015a). Short-range fluctuations represent small-scale heterogeneities, whereas  
632 long-range components capture variations in each metric at broader length scales. There is a high  
633 degree of variability within each signal that is directly related to the complex geological and  
634 geomorphological structure along the island. Within and outside the paleo-channel region,  
635 general associations between the EMI  $\sigma_a$  response and DEM metrics can be made, as we now  
636 show by ARIMA modeling. To conduct the ARIMA analysis, we chose to divide the island into  
637 three zones based on the location of the known paleo-channels. As will be discussed later, the  
638 tripartite zonation allows for a quantitative analysis of LRD at three spatial scales (regional,  
639 intermediate, local) within and outside the area containing paleo-channels. It is important to note,  
640 however, that the framework geology is likely to exhibit LRD regardless of the length-scale over  
641 which it is observed.

642

## 643 4.2 Tests for LRD

### 644 4.2.1 Tests for LRD in EMI data series

645 Both EMI spatial data series appear to be nonstationary since the mean and variance of the data  
646 fluctuate along the profile. A closer visual inspection reveals however that cyclicity is present at  
647 nearly all spatial frequencies, with the cycles superimposed in random sequence and added to a  
648 constant variance and mean (see Beran, 1994). This behavior is typical for stationary processes  
649 with LRD, and is often observed in various types of geophysical time series (Beran, 1992), for  
650 example records of Nile River stage minima (Hurst, 1951). A common first-order approach for  
651 determining whether a data series contains LRD is through inspection of the autocorrelation  
652 function, which we have computed in AutoSignal™ signal analysis software using a fast Fourier  
653 transform (FFT) algorithm (Fig. 5a, 5d). Both EMI signals exhibit large correlations at large lags  
654 (at km and higher scales), suggesting the  $\sigma_a$  responses contain LRD, or "long-memory effects" in



655 time-series language. The degree of LRD can be characterized by evaluating the scaling  
656 exponent  $H$  (or Hurst coefficient) of a self-similar process. When plotted on a log/log plot, the  
657 resulting slope of the best-fit line gives an estimate of  $H$ , where values approaching 1.0 indicate  
658 dominant long-range effects (see Beran, 1994). Results from a rescaled range  $R/S$  analysis (Fig.  
659 5b, 5e) indeed show high  $H$ -values of 0.85 ( $r^2 = 0.98$ ) and 0.95 ( $r^2 = 0.99$ ) for the 100 km and 10  
660 km surveys, indicating a strong presence of LRD at both regional and local spatial scales.

661 The manner in which different spatial frequency (i.e. wavenumber) components are  
662 superposed to constitute an observed EMI  $\sigma_a$  signal has been suggested to reveal information  
663 about the causative multi-scale geologic structure (Everett and Weiss, 2002; Weymer et al.,  
664 2015a; Beskardes et al., 2016). For example, the lowest-wavenumber contributions are  
665 associated with spatially coherent geologic features that span the longest length scales probed.  
666 The relative contributions of the various wavenumber components can be examined by plotting  
667 the  $\sigma_a$  signal power spectral density (PSD). A power-law of the form  $|\sigma_a(f)|^2 \sim f^\beta$  over several  
668 decades in spatial wavenumber is evident (Fig. 5c, 5f). The slope  $\beta$  of a power-law-shaped  
669 spectral density provides a quantitative measure of the LRD embedded in a data series and  
670 characterizes the heterogeneity, or “roughness” of the signal. A value of  $|\beta| > 1$  indicates a  
671 series that is influenced more by long-range correlations and less by small-scale fluctuations  
672 (Everett and Weiss, 2002). For comparison, a pure white noise process would have a slope of  
673 exactly  $\beta = 0$ , whereas a slope of  $\beta \sim 0.5$  indicates fractional Gaussian noise, i.e., a stationary  
674 signal with no significant long-range correlations (Everett and Weiss, 2002). The  $\beta$ -values for the  
675 100 km and 10 km surveys are  $\beta = -0.97$ , and  $\beta = -1.06$ , respectively. These results suggest that  
676 both the 100 km and 10 km EMI signals contain long-range correlations. However, there is a  
677 slightly stronger presence of LRD within the 10 km segment of the paleo-channel region  
678 compared to that within the segment that spans the entire length of the island. This indicates that  
679 long-range spatial variations in the framework geology are more important, albeit marginally so,  
680 at the 10-km scale than at the 100-km scale. It is possible that the variability within the signal  
681 and the degree of long-range correlation is also a function of the sensor footprint, relative to  
682 station spacing. This is critically examined in section 4.3.

683

684 4.2.2 Tests for LRD in surface morphometrics



685 Following the same procedure as applied to the EMI data, we performed the R/S analysis for  
686 each beach, dune, and island metric. The calculated  $H$ -values for the DEM morphometrics range  
687 between 0.80 – 0.95 with large values of  $r^2 \sim 1$ , indicating varying, but relatively strong  
688 tendencies towards LRD. Beach width and beach volume data series have  $H$ -values of 0.82 and  
689 0.86, respectively. Dune height and dune volume  $H$ -values are 0.83 and 0.80, whereas island  
690 width and island volume have higher  $H$ -values of 0.95 and 0.92, respectively. Because each data  
691 series shows moderate to strong evidence of LRD, the relative contributions of short and long-  
692 range structure contained within each signal can be further investigated by fitting ARIMA  
693 models to each data set.

694

#### 695 4.3 ARIMA statistical modeling of EMI

696 The results of the tests described in section 4.2.1 for estimating the self-similarity parameter  $H$   
697 and the slope of the PSD function suggest that both EMI data series, and by inference the  
698 underlying framework geology, exhibit LRD. Therefore, we suggest that an ARIMA process  
699 might be an appropriate model. The goal of our analysis is to estimate the  $p$ ,  $d$ , and  $q$  terms  
700 representing the order, respectively, of autoregressive (AR), integrated (I) and moving-average  
701 (MA) contributions to the signal (Box and Jenkins, 1970). For the analysis, the ‘arfima’ and  
702 ‘forecast’ statistical packages in R were used to fit a family of ARIMA ( $p,d,q$ ) models to the  
703 EMI  $\sigma_a$  data and island morphometrics (Hyndman, 2015; Hyndman and Khandakar, 2007;  
704 Veenstra, 2012). Results of ten realizations drawn from a family of ARIMA ( $p,d,q$ ) models and  
705 their residuals (RMSE) are presented in Table 1. The worst fit (ARIMA 001) models are shown  
706 for the 100 km and 10 km (Fig. 6a, 6c) surveys. The best fit (ARIMA 0d0) models for both the  
707 100 and 10 km surveys are shown in Fig. 6b and 6d, respectively. For this analysis, the tests  
708 include different combinations of  $p,d,q$  that model either short-range: ARIMA (100; 001; 101;  
709 202; 303; 404; 505), long-range: ARIMA (010; 0d0), or composite short- and long-range  
710 processes: ARIMA (111). It is important to note that AR and MA are only appropriate for “short-  
711 memory” processes since they involve only near-neighbor values to explain the current value,  
712 whereas the integration (the “I” term in ARIMA) models “long-memory” effects because it  
713 involves distant values. Note that ARIMA was developed for one-way time series, in which the  
714 arrow of time advances in only one direction, but in the current study we are using it for spatial



715 series that are reversible. Different realizations of each ARIMA ( $p,d,q$ ) data series were  
716 evaluated, enabling physical interpretations of LRD at regional, intermediate, and local spatial  
717 scales. Determining the best-fitting model is achieved by comparing the residual score, or  
718 RMSE, of each predicted data series relative to the observed data series, where lower RMSE  
719 values indicate a better fit (Table 1).

720         Based on the residuals and visual inspection of each realization, two observations are  
721 apparent: 1) both EMI data series are most accurately modeled by an ARIMA ( $0d0$ ) process with  
722 non-integer  $d$ , and 2) the mismatch between the data and their model fit is considerably lower for  
723 the 10 km survey compared to the 100 km survey. The first observation suggests that the data are  
724 most appropriately modeled by a FARIMA process; i.e., a fractional integration that is stationary  
725 ( $0 < d < 0.5$ ) and has long-range dependence (see Hosking, 1981). This implies that spatial  
726 variations in framework geology at the broadest scales dominate the EMI signal and that small-  
727 scale fluctuations in  $\sigma_a$  caused, for example, by changing hydrological conditions over brief time  
728 intervals less than the overall data acquisition interval, or fine-scale lithological variations less  
729 than a few station spacings, are not as statistically significant. Regarding the second observation,  
730 the results suggest that a small station spacing (i.e., 1 m) is preferred to accurately model both  
731 short and long-range contributions within the signal because large station spacings cannot  
732 capture short-range information. The model for the 10 km survey fits better because both  $p$  (AR)  
733 and  $q$  (MA) components increase with a smaller step-size since successive volumes of sampled  
734 subsurface overlap. On the contrary, the sensor footprint is considerably smaller than the station  
735 spacing (10 m) for the 100 km survey. Each  $\sigma_a$  measurement in that case records an independent  
736 volume of ground, yet the dataset still exhibits LRD, albeit not to the same degree as in the 10  
737 km survey.

738

#### 739 4.4 ARIMA statistical modeling of island metrics compared with EMI

740 A sequence of ARIMA ( $p,d,q$ ) models was also evaluated for the DEM morphometrics series to  
741 find best fits to the data. The analysis comprised a total of 36 model tests (Table 2). The RMSE  
742 values reveal that: 1) all data series are best fit by an ARIMA ( $0d0$ ) process with fractional  $d$ , i.e.  
743 a FARIMA process; 2) the ARIMA models, in general, more accurately fit the EMI data than the  
744 DEM morphometric data; and 3) in all cases, the poorest fit to each series is the ARIMA (001),



745 or MA process. This, in turn, means that the differencing parameter  $d$  is the most significant  
746 parameter amongst  $p$ ,  $d$  and  $q$ . It is important to note that different values of  $d$  were computed  
747 based on the best fit of each FARIMA model to the real data. A graphical representation of the  
748 FARIMA-modeled data series for each DEM metric is shown in Fig. 7, allowing a visual  
749 inspection of how well the models fit the observed data. Because each data series has its own  
750 characteristic amplitude and variability, it is not possible to compare RMSE between tests  
751 without normalization. The variance within each data series can differ by several orders of  
752 magnitude.

753 Instead of normalizing the data, a fundamentally different approach is to compare the  
754 EMI  $\sigma_a$   $d$ -values with respect to each metric at regional, intermediate, and local scales (Table 3).  
755 Higher positive  $d$ -values indicate of a stronger tendency towards LRD. It is reasonable to assume  
756 that the degree of LRD may change over smaller intermediate and/or local scales, which implies  
757 a breakdown of self-similarity. For a self-similar signal,  $d$  is a global parameter that does not  
758 depend on which segment of the series is analyzed. In other words, the  $d$ -values should be the  
759 same at all scales for a self-similar structure.

760 The results of the FARIMA analysis at the intermediate scale vary considerably within  
761 each zone of the barrier island and for each spatial data series (Table 3). In the southern zone (0 –  
762 30 km), EMI  $\sigma_a$  and beach volume have the strongest LRD ( $d = 0.44$ ), whereas the other metrics  
763 exhibit weak LRD (ranging from  $d \sim 0 - 0.2$ ), which may be characterized approximately as a  
764 white noise process. Within the paleo-channel region (30 – 60 km), all of the island metrics show  
765 a moderate to strong tendency towards LRD ( $0.3 \leq d \leq 4.2$ ), however, the EMI signal does not ( $d$   
766 = 0.11). In the northern zone (60 – 100 km) all data series contain moderate to strong LRD with  
767 the exception of beach and island width.

768 A FARIMA analysis was also conducted at the local scale by dividing the island into 10-  
769 km-segments, starting at the southern zone (0 – 10 km) and ending at the northern zone of the  
770 island (90 – 100 km). A total of 70 FARIMA model realizations were evaluated and the resulting  
771  $d$ -values demonstrate that the EMI data segments show a stronger presence of LRD ( $d > 0.4$ )  
772 within the paleo-channels (40 – 60 km) and further to the north (60 – 80 km) in close proximity  
773 to the ancestral outlet of Baffin Bay. However, there is a low  $d$ -value ( $\sim 0$ ) for the 30 – 40 km  
774 segment, which is located at the southern fringe of the Fisk (1959) paleo-channel region. These



775 findings indicate that there may be local and/or intermediate geologic controls along different  
776 parts of the island, but that the framework geology dominates beach and dune metrics at the  
777 regional scale.

778

## 779 **5 Discussion**

780 Although it has long been known that processes acting across multiple temporal and length  
781 scales permit the shape of coastlines to be described by mathematical constructs such as power  
782 law spectra and fractal dimension (Lazarus et al., 2011; Mandelbrot, 1967; Tebbens et al., 2002),  
783 analogous studies of the subsurface framework geology of a barrier island have not been carried  
784 out. For the first time, it is demonstrated that near-surface EMI geophysical methods are useful  
785 for mapping barrier island framework geology and that FARIMA data series analysis is useful  
786 for illuminating the spatial connections between subsurface geology and geomorphology. The  
787 results of the FARIMA analysis and comparisons of the best-fitting  $d$ -parameters show that  
788 beach and dune metrics closely match EMI  $\sigma_a$  responses *regionally* along the entire length of  
789 PAIS, suggesting that the long-range dependent structure of these data series is similar at large  
790 spatial scales. However, further evaluation of the  $d$ -parameters over smaller data segments  
791 reveals that there are additional intermediate and local framework geology controls on island  
792 geomorphology that are not present at the regional scale.

793         At the *intermediate* scale, a low EMI  $d$ -value ( $d = 0.11$ ) suggests there is only a weak  
794 framework-geologic control on barrier island morphometrics. A possible explanation is that the  
795 paleo-channels, located within a  $\sim 30$  km segment of the island, are not regularly spaced and on  
796 average are less than a few km wide. This implies that the framework geology controls are  
797 localized (i.e., effective in shaping island geomorphology only at smaller spatial scales). At the  
798 *local* scale, relationships between the long-range-dependence of EMI and each metric vary  
799 considerably, but the  $d$ -values demonstrate that the EMI data segments show a stronger presence  
800 of LRD ( $d > 0.4$ ) within the paleo-channels (40 – 60 km) and further to the north (60 – 80 km) in  
801 close proximity to the ancestral outlet of the Baffin Bay. The two networks of paleo-channels  
802 that are located just outside of the 30 – 40 km segment may explain the low EMI  $d$ -value ( $d \sim 0$ )  
803 calculated for this segment. In other words, the channels do not occupy most of the 30 – 40 km  
804 segment, thus resulting in a lower  $d$ -value. It is hypothesized that the alongshore projection of



805 the geometry of each channel is directly related to a corresponding variation in the EMI signal,  
806 such that large, gradual minima in  $\sigma_a$  are indicative of large, deep channel cross-sections and  
807 small, abrupt minima in  $\sigma_a$  represent smaller, shallow channel cross-sections. At shallower  
808 depths within the DOI probed by the EMI sensor, variability in the  $\sigma_a$  signal may correspond to  
809 changes in sediment characteristics as imaged by GPR (Fig. 3). Located beneath a washover  
810 channel, a zone of high conductivity EMI  $\sigma_a$  responses between  $\sim 450 - 530$  m coincides with a  
811 segment of the GPR section where the signal is more attenuated and lacks the fine stratification  
812 that correlates much better with the lower  $\sigma_a$  zones. The contrasts in lithology between the  
813 overwash deposits and stratified infilled sands was detected by both EMI and GPR  
814 measurements, suggesting that EMI is a useful tool for mapping variations in barrier island  
815 framework geology.

816 It is argued herein that differences in the  $d$  parameter between EMI  $\sigma_a$  readings (our  
817 assumed proxy for framework geology) and LiDAR-derived surface morphometrics provide a  
818 new metric that is useful for quantifying the causative physical processes that govern island  
819 transgression across multiple spatial scales. All of the calculated  $d$ -values in this study are  
820 derived from ARIMA ( $0d0$ ) models that fit the observations, and lie within the range of  $0 < d <$   
821  $0.5$ , suggesting that each data series is stationary but does contain long-range structure that  
822 represents randomly-placed cyclicities in the data. For all models in our study, the  $d$ -values range  
823 between ( $\sim 0 - 0.50$ ), which enables a geomorphological interpretation of the degree of LRD and  
824 self-similarity at different spatial scales. In other words, the  $d$ -parameter not only provides an  
825 indication of the scale dependencies within the data, but also offers a compact way for analyzing  
826 the statistical connections between free (weaker  $d \sim 0$ ) or forced (stronger  $d \sim 0.5$ )  
827 geomorphological evolution along the island.

828 Alongshore variations in beach width and dune height are not uniform in PAIS and  
829 exhibit different spatial structure within and outside the paleo-channel region (Fig. 5). These  
830 dissimilarities may be forced by the framework geology within the central zone of the island but  
831 are influenced more by contemporary morphodynamic processes outside the paleo-channel  
832 region. Once the dunes are initialized in part by the framework geology, stabilizing vegetation  
833 may act as another important control on beach-dune evolution alongshore (Hesp, 1988). This  
834 effect could be represented by higher-wavenumber components embedded within the spatial data



835 series. Beach and dune morphology in areas that are not controlled by framework geology (e.g.,  
836 the northern and southern zones) exhibit more small-scale fluctuations representing a free system  
837 primarily controlled by contemporary morphodynamics (e.g., wave action, storm surge, wind,  
838 etc.). Because variations in dune height exert an important control on storm impacts (Sallenger,  
839 2000) and ultimately large-scale island transgression (Houser, 2012), it is argued here that the  
840 framework geology of PAIS acts as an important control on island response to storms and sea-  
841 level rise. The forced behavior within the paleo-channel region challenges existing models that  
842 consider only small-scale undulations in the dune line that are caused by natural randomness  
843 within the system. Rather, we propose that dune growth is forced by the framework geology,  
844 whose depth is related to the thickness of the modern shoreface sands beneath the beach. This  
845 depth is the primary quantity that is detected by the EMI sensor.

846 Our findings extend previous framework geology studies from the Outer Banks, NC (e.g.,  
847 Browder and McNinch, 2006; McNinch, 2004; Riggs et al., 1995), Fire Island, NY (e.g., Hapke  
848 et al., 2010; Lentz and Hapke, 2011), and Pensacola, FL (e.g., Houser, 2012) where feedbacks  
849 between geologic features and relict sediments within the littoral system have been shown to act  
850 as an important control on dune growth and evolution. Nonetheless, most of these studies focus  
851 on offshore controls on shoreface and/or beach-dune dynamics at either local or intermediate  
852 scales because few islands worldwide exist that are as long and/or continuous as North Padre  
853 Island. The current study augments the existing literature in that 1) it outlines a quantitative  
854 method for determining *free* and *forced* evolution of barrier island geomorphology at multiple  
855 length scales, and 2) it demonstrates that there is a first-order control on dune height at the local  
856 scale within an area of known paleo-channels, suggesting that framework geology controls are  
857 localized within certain zones of PAIS.

858 Further study is required to determine how this combination of free- and forced-behavior  
859 resulting from the variable and localized framework geology affects island transgression.  
860 Methods of data analysis that would complement the techniques presented in this paper might  
861 include; spatiotemporal modeling, power spectral analysis, wavelet decomposition, bicoherence  
862 analysis, and wavelet coherence. These approaches would provide important information  
863 regarding:



- 864 1. Coherence and phase relationships between subsurface structure and island  
865 geomorphology.
- 866 2. Non-linear interactions of coastal processes across large and small spatiotemporal  
867 scales.

868 Quantifying and interpreting the significance of framework geology as a driver of barrier island  
869 formation and evolution and its interaction with contemporary morphodynamic processes is  
870 essential for designing and sustainably managing resilient coastal communities and habitats.

871

## 872 **6 Conclusions**

873 This study demonstrates the utility of EMI geophysical profiling as a new tool for mapping the  
874 length-scale dependence of barrier island framework geology and introduces the importance of  
875 statistical modeling of geophysical and geomorphological spatial data series by FARIMA  
876 analysis to better understand the geologic controls on large-scale barrier island transgression.  
877 The EMI and morphometric data series exhibit LRD to varying degrees, and each can be  
878 accurately modeled using a non-integral parameter  $d$ . The value of this parameter diagnoses the  
879 spatial relationship between the framework geology and surface geomorphology. At the *regional*  
880 *scale* (~100 km), small differences in  $d$  between the EMI and morphometrics series suggest that  
881 the long-range-dependent structure of each data series with respect to EMI  $\sigma_a$  is statistically  
882 similar. At the *intermediate scale* (~ 30 km), there is a greater difference between the  $d$ -values of  
883 the EMI and island metrics within the known paleo-channel region, suggesting a more localized  
884 geologic control with less contributions from broader-scale geological structures. At the *local*  
885 *scale* (10 km), there is a considerable degree of variability between the  $d$ -values of the EMI and  
886 each metric. These results all point toward a forced barrier-island evolutionary behavior within  
887 the paleo-channel region transitioning into a free, or scale-independent behavior dominated by  
888 contemporary morphodynamics outside the paleo-channel region. The results from this study  
889 suggest that the framework geology initially controls the development of the dunes at the local  
890 scale within the paleo-channel region. This means that barrier island geomorphology at PAIS is  
891 forced and scale-dependent, unlike shorelines which have been shown at other barrier islands to  
892 be scale-independent (Tebbens et al., 2002; Lazarus et al., 2011). Our findings reveal that  
893 shorelines may have different irregularity than island geomorphology, which suggests an



894 alongshore redistribution of sediment that shapes the shoreline toward a more dissipative state  
895 over time. Without local variations in the framework geology alongshore, small-scale variations  
896 in the shoreline will be masked by the large-scale transport gradients over long timescales. The  
897 exchange of sediment amongst nearshore, beach and dune in areas outside the paleo-channel  
898 region is scale independent, meaning that barrier islands like PAIS exhibit a combination of free  
899 and forced behaviors that will affect the response of the island to sea level rise and storms. We  
900 propose that our analysis is not limited to PAIS but can be applied to other barrier islands and  
901 potentially in different geomorphic environments, both coastal and inland.

902

903 **Competing interests.** The authors declare that they have no conflict of interest.

904

#### 905 **Acknowledgments**

906 We are grateful to Patrick Barrineau, Andy Evans, Brianna Hammond Williams, Alex van  
907 Plantinga, and Michael Schwind for their assistance in the field. All data in this study are  
908 available by contacting the corresponding author: [brad.weymer@gmail.com](mailto:brad.weymer@gmail.com). The field data  
909 presented in this manuscript was collected under the National Park Service research permit:  
910 #PAIS-2013-SCI-0005. This research was funded in part by Grants-in-Aid of Graduate Student  
911 Research Award by the Texas Sea Grant College Program.

912

913

914

915

916

917

918

919

920

921

922

923



924 **References**

925

926 Anderson, J. B., Wallace, D. J., Simms, A. R., Rodriguez, A. B., Weight, R. W., and Taha, Z. P.,  
927 2015. Recycling sediments between source and sink during a eustatic cycle: Systems of  
928 late Quaternary northwestern Gulf of Mexico Basin. *Earth-Science Reviews* 153, 111-138.

929 Andrie, R., 1996. The west coast of Britain: Statistical self-similarity vs. characteristic scales in  
930 the landscape. *Earth Surface Processes and Landforms*, 21(10), 955-962.

931 Bailey, R. J., and Smith, D. G., 2005. Quantitative evidence for the fractal nature of the  
932 stratigraphic record: results and implications. *Proceedings of the Geologists' Association*,  
933 116(2), 129-138.

934 Bassingthwaite, J. B., and Raymond, G. M., 1994. Evaluating rescaled range analysis for time  
935 series. *Annals of biomedical engineering*, 22(4), 432-444.

936 Belknap, D. F., and Kraft, J. C., 1985. Influence of antecedent geology on stratigraphic  
937 preservation potential and evolution of Delaware's barrier systems. *Marine geology*, 63(1),  
938 235-262.

939 Beran, J., 1992. Statistical methods for data with long-range dependence. *Statistical Science*, 7(4),  
940 404-427.

941 Beran, J., 1994. *Statistics for long-memory processes (Vol. 61)*: CRC Press.

942 Beskardes, G. D., Weiss, C. J., and Everett, M. E., 2016. Estimating the power-law distribution of  
943 Earth electrical conductivity from low-frequency, controlled-source electromagnetic  
944 responses. *Geophysical Journal International*, 208(2), 639-651.

945 Box, G. E., and Jenkins, G. M., 1970. *Time series analysis: forecasting and control* Holden-Day,  
946 San Francisco, CA.

947 Browder, A. G., and McNinch, J. E., 2006. Linking framework geology and nearshore morphology:  
948 correlation of paleo-channels with shore-oblique sandbars and gravel outcrops. *Marine*  
949 *geology*, 231(1), 141-162.

950 Brown, L. F., and Macon, J., 1977. *Environmental geologic atlas of the Texas coastal zone:*  
951 *Kingsville area*: Bureau of Economic Geology, University of Texas at Austin.

952 Burrough, P., 1981. Fractal dimensions of landscapes and other environmental data. *Nature*,  
953 294(5838), 240-242.



- 954 Buynevich, I. V., FitzGerald, D. M., and van Heteren, S., 2004. Sedimentary records of intense  
955 storms in Holocene barrier sequences, Maine, USA. *Marine Geology*, 210(1), 135-148.
- 956 Cimino, G., Del Duce, G., Kadonaga, L., Rotundo, G., Sisani, A., Stabile, G., . . . Whiticar, M.,  
957 1999. Time series analysis of geological data. *Chemical Geology*, 161(1), 253-270.
- 958 Coleman, J. M., and Gagliano, S. M., 1964. Cyclic sedimentation in the Mississippi River deltaic  
959 plain.
- 960 Colman, S. M., Halka, J. P., Hobbs, C., Mixon, R. B., and Foster, D. S., 1990. Ancient channels  
961 of the Susquehanna River beneath Chesapeake Bay and the Delmarva Peninsula.  
962 *Geological Society of America Bulletin*, 102(9), 1268-1279.
- 963 De Jong, P., and Penzer, J., 1998. Diagnosing shocks in time series. *Journal of the American*  
964 *Statistical Association*, 93(442), 796-806.
- 965 Delefortrie, S., Saey, T., Van De Vijver, E., De Smedt, P., Missiaen, T., Demerre, I., and Van  
966 Meirvenne, M., 2014. Frequency domain electromagnetic induction survey in the  
967 intertidal zone: Limitations of low-induction-number and depth of exploration. *Journal of*  
968 *Applied Geophysics*, 100, 14-22.
- 969 Demarest, J. M., and Leatherman, S. P., 1985. Mainland influence on coastal transgression:  
970 Delmarva Peninsula. *Marine geology*, 63(1), 19-33.
- 971 Doukhan, P., Oppenheim, G., and Taqqu, M. S., 2003. Theory and applications of long-range  
972 dependence: Birkhauser.
- 973 Eke, A., Herman, P., Bassingthwaighte, J., Raymond, G., Percival, D., Cannon, M., . . . Ikrényi,  
974 C., 2000. Physiological time series: distinguishing fractal noises from motions. *Pflügers*  
975 *Archiv*, 439(4), 403-415.
- 976 Evans, M., W, Hine, A., C, Belknap, D., F, and Davis, R., A., 1985. Bedrock controls on barrier  
977 island development: west-central Florida coast. *Marine geology*, 63(1-4), 263-283.
- 978 Evans, R. L., and Lizarralde, D., 2011. The competing impacts of geology and groundwater on  
979 electrical resistivity around Wrightsville Beach, NC. *Continental Shelf Research*, 31(7),  
980 841-848.
- 981 Everett, M. E., and Weiss, C. J., 2002. Geological noise in near-surface electromagnetic induction  
982 data. *Geophysical Research Letters*, 29(1), 10-11-10-14.
- 983 Everett, M. E., 2013. Near-surface applied geophysics. Cambridge University Press.



- 984 Fisk, H. N., 1959. Padre Island and Laguna Madre Flats, coastal south Texas. Proceedings 2nd  
985 Coastal Geography Conference, Louisiana State University, Baton Rouge, LA, 103-151.
- 986 Fitterman, D. V., and Stewart, M. T., 1986. Transient electromagnetic sounding for groundwater.  
987 Geophysics, 51(4), 995-1005.
- 988 Frazier, D. E., 1967. Recent deltaic deposits of the Mississippi River: their development and  
989 chronology.
- 990 Geophysical Survey Systems Incorporated., 2007. Profiler EMP-400 user's manual, Geophysical  
991 Survey Systems, Incorporated, User's Manual.
- 992 Granger, C. W., and Joyeux, R., 1980. An introduction to long-memory time series models and  
993 fractional differencing. Journal of time series analysis, 1(1), 15-29.
- 994 Guillemoteau, J., and Tronicke, J., 2015. Non-standard electromagnetic induction sensor  
995 configurations: Evaluating sensitivities and applicability. Journal of Applied Geophysics,  
996 118, 15-23.
- 997 Gutierrez, B. T., Plant, N. G., Thieler, E. R., and Turecek, A., 2015. Using a Bayesian network to  
998 predict barrier island geomorphologic characteristics. Journal of Geophysical Research:  
999 Earth Surface, 120(12), 2452-2475.
- 1000 Hapke, C. J., Kratzmann, M. G., and Himmelstoss, E. A., 2013. Geomorphic and human influence  
1001 on large-scale coastal change. Geomorphology, 199, 160-170.
- 1002 Hapke, C. J., Lentz, E. E., Gayes, P. T., McCoy, C. A., Hehre, R., Schwab, W. C., and Williams,  
1003 S. J., 2010. A review of sediment budget imbalances along Fire Island, New York: can  
1004 nearshore geologic framework and patterns of shoreline change explain the deficit? Journal  
1005 of Coastal Research, 510-522.
- 1006 Hapke, C. J., Plant, N. G., Henderson, R. E., Schwab, W. C., and Nelson, T. R., 2016. Decoupling  
1007 processes and scales of shoreline morphodynamics. Marine geology, 381, 42-53.
- 1008 Hesp, P., 1988. Morphology, dynamics and internal stratification of some established foredunes in  
1009 southeast Australia. Sedimentary Geology, 55(1-2), 17-41.
- 1010 Honeycutt, M. G., and Krantz, D. E., 2003. Influence of the geologic framework on spatial  
1011 variability in long-term shoreline change, Cape Henlopen to Rehoboth Beach, Delaware.  
1012 Journal of Coastal Research, 147-167.
- 1013 Hosking, J. R., 1981. Fractional differencing. Biometrika, 68(1), 165-176.



- 1014 Houser, C., Hapke, C., and Hamilton, S., 2008. Controls on coastal dune morphology, shoreline  
1015 erosion and barrier island response to extreme storms. *Geomorphology*, 100(3), 223-240.
- 1016 Houser, C., and Mathew, S., 2011. Alongshore variation in foredune height in response to transport  
1017 potential and sediment supply: South Padre Island, Texas. *Geomorphology*, 125(1), 62-72.
- 1018 Houser, C., 2012. Feedback between ridge and swale bathymetry and barrier island storm response  
1019 and transgression. *Geomorphology*, 173, 1-16.
- 1020 Houser, C., 2013. Alongshore variation in the morphology of coastal dunes: Implications for storm  
1021 response. *Geomorphology*, 199, 48-61.
- 1022 Houser, C., Wernette, P., Rentschlar, E., Jones, H., Hammond, B., and Trimble, S., 2015. Post-  
1023 storm beach and dune recovery: Implications for barrier island resilience.  
1024 *Geomorphology*, 234, 54-63.
- 1025 Hurst, H. E., 1951. Long-term storage capacity of reservoirs. *Trans. Amer. Soc. Civil Eng.*, 116,  
1026 770-808.
- 1027 Hyndman, R. J., 2015. Forecasting functions for time series and linear models. R package version  
1028 5.9., URL:<http://github.com/robjhyndman/forecast>.
- 1029 Hyndman, R. J., and Khandakar, Y., 2007. Automatic time series for forecasting: the forecast  
1030 package for R. Retrieved from
- 1031 Jol, H. M., Smith, D. G., and Meyers, R. A., 1996. Digital ground penetrating radar (GPR): a new  
1032 geophysical tool for coastal barrier research (Examples from the Atlantic, Gulf and Pacific  
1033 coasts, USA). *Journal of Coastal Research*, 960-968.
- 1034 Jol, H. M. (Ed.), 2008. *Ground penetrating radar theory and applications*. Elsevier.
- 1035 Kraft, J., Belknap, D., McDonald, K., Maley, K., and Marx, P., 1982. Models of a shoreface-  
1036 nearshore marine transgression over estuarine and barrier systems and antecedent  
1037 topography of the Atlantic coast. Paper presented at the Geol. Soc. Am., Abstr. With  
1038 Programs.
- 1039 Lazarus, E., Ashton, A., Murray, A. B., Tebbens, S., and Burroughs, S., 2011. Cumulative versus  
1040 transient shoreline change: Dependencies on temporal and spatial scale. *Journal of*  
1041 *Geophysical Research: Earth Surface* (2003–2012), 116(F2).



- 1042 Lentz, E. E., and Hapke, C. J., 2011. Geologic framework influences on the geomorphology of an  
1043 anthropogenically modified barrier island: Assessment of dune/beach changes at Fire  
1044 Island, New York. *Geomorphology*, 126(1), 82-96.
- 1045 Lentz, E. E., Hapke, C. J., Stockdon, H. F., and Hehre, R. E., 2013. Improving understanding of  
1046 near-term barrier island evolution through multi-decadal assessment of morphologic  
1047 change. *Marine geology*, 337, 125-139.
- 1048 Linden, A., Adams, J. L., and Roberts, N., 2003. Evaluating disease management program  
1049 effectiveness: an introduction to time-series analysis. *Disease Management*, 6(4), 243-255.
- 1050 Malamud, B. D., and Turcotte, D. L., 1999. Self-affine time series: I. Generation and  
1051 analyses. *Advances in Geophysics*, 40, 1-90.
- 1052 Mandelbrot, B. B., 1967. How long is the coast of Britain. *Science*, 156(3775), 636-638.
- 1053 Mandelbrot, B. B., and Taqqu, M. S., 1979. Robust R/S analysis of long run serial correlation:  
1054 IBM Thomas J. Watson Research Division.
- 1055 McNinch, J. E., 2004. Geologic control in the nearshore: shore-oblique sandbars and shoreline  
1056 erosional hotspots, Mid-Atlantic Bight, USA. *Marine geology*, 211(1), 121-141.
- 1057 Miselis, J. L., Buster, N. A., and Kindinger, J. L., 2014. Refining the link between the Holocene  
1058 development of the Mississippi River Delta and the geologic evolution of Cat Island, MS:  
1059 implications for delta-associated barrier islands. *Marine geology*, 355, 274-290.
- 1060 Miselis, J. L., and McNinch, J. E., 2006. Calculating shoreline erosion potential using nearshore  
1061 stratigraphy and sediment volume: Outer Banks, North Carolina. *Journal of Geophysical  
1062 Research: Earth Surface*, 111(F2).
- 1063 Morton, R. A., and Sallenger Jr, A. H., 2003. Morphological impacts of extreme storms on sandy  
1064 beaches and barriers. *Journal of Coastal Research*, 560-573.
- 1065 Murray, A. B., and Thieler, E. R., 2004. A new hypothesis and exploratory model for the formation  
1066 of large-scale inner-shelf sediment sorting and “rippled scour depressions”. *Continental  
1067 Shelf Research*, 24(3), 295-315.
- 1068 Neal, A., 2004. Ground-penetrating radar and its use in sedimentology: principles, problems and  
1069 progress. *Earth-science reviews*, 66(3), 261-330.
- 1070 Nobes, D. C., 1996. Troubled waters: Environmental applications of electrical and  
1071 electromagnetic methods. *Surveys in Geophysics*, 17(4), 393-454.



- 1072 NOAA., 2015a. National Hurricane Center. Data set accessed 29 April 2015 at  
1073 <http://www.nhc.noaa.gov/data/>.
- 1074 NOAA., 2015b. Tides and Currents. <https://tidesandcurrents.noaa.gov>, accessed 18 October, 2015.
- 1075 NOAA., 2017. Digital Coast. <https://coast.noaa.gov/digitalcoast/>, accessed 31 October, 2017.
- 1076 Nummedal, D., and Swift, D. J., 1987. Transgressive stratigraphy at sequence-bounding  
1077 unconformities: some principles derived from Holocene and Cretaceous examples.
- 1078 Otvos, E. G., and Giardino, M. J., 2004. Interlinked barrier chain and delta lobe development,  
1079 northern Gulf of Mexico. *Sedimentary Geology*, 169(1), 47-73.
- 1080 Radliński, A., Radlińska, E., Agamalian, M., Wignall, G., Lindner, P., and Randl, O., 1999. Fractal  
1081 geometry of rocks. *Physical Review Letters*, 82(15), 3078.
- 1082 Riggs, S. R., Cleary, W. J., and Snyder, S. W., 1995. Influence of inherited geologic framework  
1083 on barrier shoreface morphology and dynamics *Marine geology* (Vol. 126, pp. 213-234).
- 1084 Rodriguez, A. B., Fassell, M. L., and Anderson, J. B., 2001. Variations in shoreface progradation  
1085 and ravinement along the Texas coast, Gulf of Mexico. *Sedimentology*, 48(4), 837-853.
- 1086 Sallenger Jr, A. H., 2000. Storm impact scale for barrier islands. *Journal of Coastal Research*, 16(3),  
1087 890-895.
- 1088 Samorodnitsky, G., 2007. Long range dependence. *Foundations and Trends in Stochastic Systems*,  
1089 1(3), 163-257.
- 1090 Santos, V. R., Porsani, J. L., Mendonça, C. A., Rodrigues, S. I., and DeBlasis, P. D., 2009.  
1091 Reduction of topography effect in inductive electromagnetic profiles: application on  
1092 coastal sambaqui (shell mound) archaeological site in Santa Catarina state, Brazil.  
1093 *Journal of Archaeological Science*, 36(10), 2089-2095.
- 1094 Schlager, W., 2004. Fractal nature of stratigraphic sequences. *Geology*, 32(3), 185-188.
- 1095 Schupp, C. A., McNinch, J. E., and List, J. H., 2006. Nearshore shore-oblique bars, gravel outcrops,  
1096 and their correlation to shoreline change. *Marine geology*, 233(1), 63-79.
- 1097 Schwab, W. C., Baldwin, W. E., Hapke, C. J., Lentz, E. E., Gayes, P. T., Denny, J. F., . . . Warner,  
1098 J. C., 2013. Geologic evidence for onshore sediment transport from the inner continental  
1099 shelf: Fire Island, New York. *Journal of Coastal Research*, 29(3), 526-544.
- 1100 Schwab, W. C., Thieler, E. R., Allen, J. R., Foster, D. S., Swift, B. A., and Denny, J. F., 2000.  
1101 Influence of inner-continental shelf geologic framework on the evolution and behavior of



- 1102 the barrier-island system between Fire Island Inlet and Shinnecock Inlet, Long Island, New  
1103 York. *Journal of Coastal Research*, 408-422.
- 1104 Seijmonsbergen, A. C., Biewinga, D. T., and Pruijssers, A. P., 2004. A geophysical profile at the  
1105 foot of the Dutch coastal dunes near the former outlet of the ‘Old Rhine’. *Netherlands*  
1106 *Journal of Geosciences*, 83(4), 287-291.
- 1107 Stewart, M. T., 1982. Evaluation of electromagnetic methods for rapid mapping of salt-water  
1108 interfaces in coastal aquifers. *Groundwater*, 20(5), 538-545.
- 1109 Stone, G. W., Liu, B., Pepper, D. A., and Wang, P., 2004. The importance of extratropical and  
1110 tropical cyclones on the short-term evolution of barrier islands along the northern Gulf of  
1111 Mexico, USA. *Marine Geology*, 210(1), 63-78.
- 1112 Swarzenski, P. W., and Izbicki, J. A., 2009. Coastal groundwater dynamics off Santa Barbara,  
1113 California: Combining geochemical tracers, electromagnetic seepmeters, and electrical  
1114 resistivity. *Estuarine, Coastal and Shelf Science*, 83(1), 77-89.
- 1115 Talley, D. M., North, E. W., Juhl, A. R., Timothy, D. A., Conde, D., Jody, F., . . . Hall, C. J., 2003.  
1116 Research challenges at the land–sea interface. *Estuarine, Coastal and Shelf Science*, 58(4),  
1117 699-702.
- 1118 Tamura, T., 2012. Beach ridges and prograded beach deposits as palaeoenvironment  
1119 records. *Earth-Science Reviews*, 114(3), 279-297.
- 1120 Taqqu, M. S., 2003. Fractional Brownian motion and long-range dependence. Theory and  
1121 applications of long-range dependence, 5-38.
- 1122 Taqqu, M. S., Teverovsky, V., and Willinger, W., 1995. Estimators for long-range dependence: an  
1123 empirical study. *Fractals*, 3(04), 785-798.
- 1124 Tebbens, S. F., Burroughs, S. M., and Nelson, E. E., 2002. Wavelet analysis of shoreline change  
1125 on the Outer Banks of North Carolina: An example of complexity in the marine sciences.  
1126 *Proceedings of the National Academy of Sciences*, 99(suppl 1), 2554-2560.
- 1127 Twichell, D. C., Flocks, J. G., Pendleton, E. A., and Baldwin, W. E., 2013. Geologic controls on  
1128 regional and local erosion rates of three northern Gulf of Mexico barrier-island systems.  
1129 *Journal of Coastal Research*, 63(sp1), 32-45.
- 1130 Veenstra, J., 2012. Persistence and Anti-persistence: Theory and Software. Ph.D. Thesis, Western  
1131 University.



- 1132 Weise, B. R., and White, W. A., 1980. Padre Island National Seashore: A guide to the geology,  
1133 natural environments, and history of a Texas barrier island (Vol. 17). Bureau of Economic  
1134 Geology, University of Texas at Austin.
- 1135 Wernette, P., Houser, C., and Bishop, M. P., 2016. An automated approach for extracting Barrier  
1136 Island morphology from digital elevation models. *Geomorphology*, 262, 1-7.
- 1137 Weymer, B. A., Everett, M. E., de Smet, T. S., and Houser, C., 2015a. Review of electromagnetic  
1138 induction for mapping barrier island framework geology. *Sedimentary Geology*, 321, 11-  
1139 24.
- 1140 Weymer, B. A., Everett, M. E., Houser, C., Wernette, P., and Barrineau, P., 2016. Differentiating  
1141 tidal and groundwater dynamics from barrier island framework geology: Testing the utility  
1142 of portable multi-frequency EMI profilers. *Geophysics*, 81, E347-E361.
- 1143 Weymer, B. A., Houser, C., and Giardino, J. R., 2015b. Poststorm Evolution of Beach-Dune  
1144 Morphology: Padre Island National Seashore, Texas. *Journal of Coastal Research*, 31(3),  
1145 634 – 644.
- 1146 Xu, T., Moore, I. D., and Gallant, J. C., 1993. Fractals, fractal dimensions and landscapes—a  
1147 review. *Geomorphology*, 8(4), 245-262.
- 1148  
1149  
1150  
1151  
1152  
1153  
1154  
1155  
1156  
1157  
1158  
1159  
1160  
1161



1162 **Tables**

1163 **Table 1.** Comparison of residuals (RMSE) of each ARIMA model for the 100 km and 10 km  
1164 EMI surveys.

	<b>EMI (100 km)</b>	<b>EMI (10 km)</b>
<b>ARIMA (100)</b>	18.4	8.14
<b>ARIMA (001)</b>	49.7	41.1
<b>ARIMA (101)</b>	15.6	6.65
<b>ARIMA (202)</b>	40.6	7.31
<b>ARIMA (303)</b>	40.5	7.22
<b>ARIMA (404)</b>	40.3	7.22
<b>ARIMA (505)</b>	40.2	7.29
<b>ARIMA (111)</b>	15.8	5.72
<b>ARIMA (010)</b>	18.5	8.15
<b>ARIMA (0d0)</b>	15.5	5.55

1165

1166

1167

1168

1169

1170

1171

1172

1173

1174

1175

1176

1177

1178

1179

1180



1181 **Table 2.** Comparison of residuals (RMSE) of each ARIMA model for all spatial data series.  
 1182 Note that the residuals for each DEM metric correspond to the analysis performed at the regional  
 1183 scale (i.e., 100 km).

	ARIMA (100)	ARIMA (001)	ARIMA (101)	ARIMA (111)	ARIMA (010)	ARIMA (0d0)
<b>Beach width</b>	13.4	14.9	13.0	13.1	14.8	13.0
<b>Beach volume</b>	44.8	50.5	43.1	43.1	49.1	42.7
<b>Dune height</b>	0.7	0.8	0.7	0.7	0.8	0.7
<b>Dune volume</b>	60.6	63.9	59.7	59.2	69.03	58.9
<b>Island width</b>	138.4	253.2	121.3	121.1	140.8	120.9
<b>Island volume</b>	271.3	611.4	244.3	244.1	273.9	243.3

1184  
 1185  
 1186  
 1187  
 1188  
 1189  
 1190  
 1191  
 1192  
 1193  
 1194  
 1195  
 1196  
 1197  
 1198  
 1199  
 1200  
 1201



1202 **Table 3.** Summary table showing the computed *d* parameters that most appropriately model each  
1203 ARIMA (0*d*0) iteration (i.e., lowest RMSE).

Alongshore distance	Beach width	Beach volume	Dune height	Dune volume	Island width	Island volume	EMI $\sigma_a$
<b>“Regional”</b>							
<b>0-100 km</b>	0.38	0.42	0.34	0.32	0.13	~0.00	0.35
<b>“Intermediate”</b>							
<b>0-30 km</b>	~0.00	0.44	0.13	0.20	0.03	0.18	0.44
<b>30-60 km</b>	0.37	0.30	0.36	0.31	0.30	0.42	0.11
<b>60-100 km</b>	0.26	0.41	0.35	0.46	~0.00	0.50	0.49
<b>“Local”</b>							
<b>0-10 km</b>	0.41	0.39	0.20	0.21	0.09	0.18	0.36
<b>10-20 km</b>	0.30	0.42	0.20	0.26	0.37	~ 0.00	0.36
<b>20-30 km</b>	0.26	0.40	~ 0.00	~ 0.00	0.49	~ 0.00	~ 0.00
<b>30-40 km</b>	0.47	~ 0.00	0.41	0.25	0.29	0.28	~ 0.00
<b>40-50 km</b>	0.28	0.21	0.21	0.19	0.30	0.02	0.44
<b>50-60 km</b>	0.03	0.31	0.23	0.32	~ 0.00	0.33	0.48
<b>60-70 km</b>	0.16	0.37	0.29	0.34	~ 0.00	0.30	0.40
<b>70-80 km</b>	0.47	0.34	0.43	0.26	~ 0.00	0.42	0.49
<b>80-90 km</b>	0.27	0.19	0.42	0.39	0.01	0.02	~ 0.00
<b>90-100 km</b>	0.13	0.13	~ 0.00	0.06	0.44	0.47	0.41

1204

1205

1206

1207

1208

1209

1210

1211

1212

1213

1214

1215

1216



1217 **Figure Captions:**

1218

1219 **Figure 1.** Location map and DEM of the study area at Padre Island National Seashore (PAIS),  
1220 Texas, USA. Elevations for the DEM are reported as meters above sea level (masl). Field images  
1221 from the northern (N), central (C), and southern (S) regions of the island showing alongshore  
1222 differences in beach-dune morphology. Note: views are facing north for the northern and  
1223 southern locations, and the central location view is to the south. Images taken in October, 2014.

1224

1225 **Figure 2.** 100 km (a) and 10 km (b) alongshore EMI surveys showing DEM's of study area and  
1226 previously identified paleo-channel region by Fisk (1959). Channels are highlighted in red and  
1227 green, where the green region indicates the location of the 10 km survey. 25 ft (7.6 m) contour  
1228 intervals are highlighted with depths increasing from yellow to red and the center of the channels  
1229 are represented by the black-dotted lines. For each survey, raw  $\sigma_a$  and zero-mean drift-corrected  
1230 EMI responses are shown in grey and black, respectively. Tidal conditions during each EMI  
1231 acquisition segment are shown below each panel. Low (lt) and falling tides (ft) are indicated by  
1232 blue and light blue shades, respectively. High (ht) and rising tides (rt) are highlighted in red and  
1233 light red, respectively.

1234

1235 **Figure 3.** Comparison of EMI  $\sigma_a$  responses from the 100 km survey with 100 MHz GPR data  
1236 within one of the Fisk (1959) paleo-channels. The 800 m segment (A – A') crosses a smaller  
1237 stream within the network of paleo-channels in the central zone of PAIS. The DOI of the 3 kHz  
1238 EMI responses is outlined by the red box on the lower GPR radargram.

1239

1240 **Figure 4.** DEM metrics extracted from aerial LiDAR data. The sampling interval (step-size) for  
1241 each data series is 10 m and the coordinates are matched with each EMI acquisition point. Each  
1242 panel corresponds to a) beach width, b) beach volume, c) dune height, d) dune volume, e) island  
1243 width, f) island volume, and g) EMI  $\sigma_a$ . The island is divided into three zones (red vertical lines)  
1244 roughly indicating the locations within and outside the known paleo-channel region. A Savitzky-  
1245 Golay smoothing filter was applied to all data series (LiDAR and EMI) using a moving window  
1246 of  $n = 250$  to highlight the large-scale patterns in each signal.

1247

1248 **Figure 5.** Autocorrelations of  $\sigma_a$  for the 100 km (a) and 10 km EMI surveys (d). *R/S* analysis for  
1249 the 100 km (b) and 10 km surveys (e). PSD plots for the 100 km (c) and 10 km surveys (f).

1250

1251 **Figure 6.** Examples of the worst (6a, 6c) and best (6b, 6d) fit ARIMA models for the 100 and 10  
1252 km EMI surveys. Model results are shown for the processed (drift-corrected)  $\sigma_a$  data. Residuals  
1253 (RMSE) listed for each model gives the standard deviation of the model prediction error. For  
1254 each plot, original data is in red and fitted (model) data is in blue.

1255

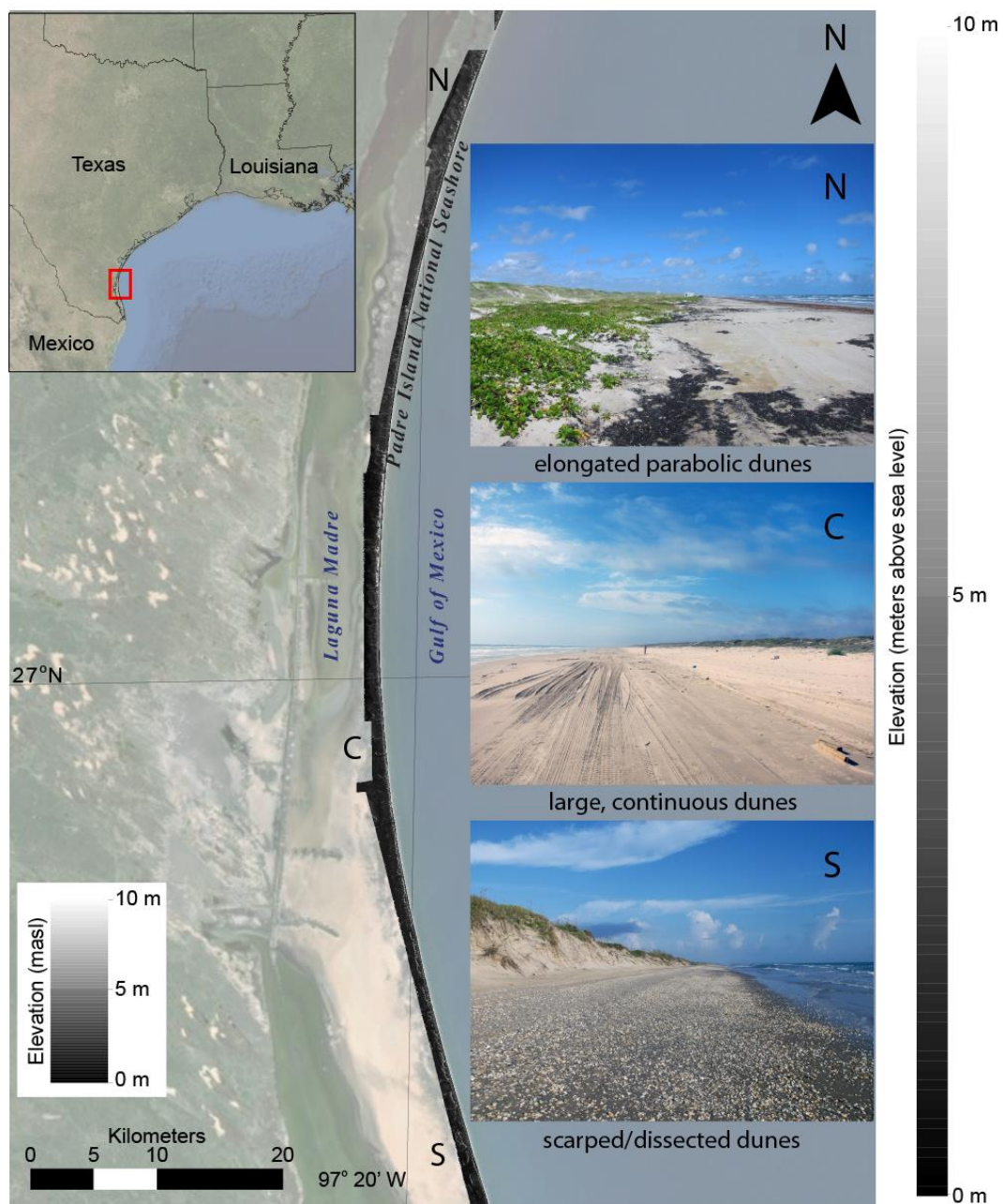
1256 **Figure 7.** Example of the best fit ARIMA (0d0) models for each LiDAR-derived DEM metric: a)  
1257 beach width, b) beach volume, c) dune height, d) dune volume, e) island width, f) island volume.

1258

1259

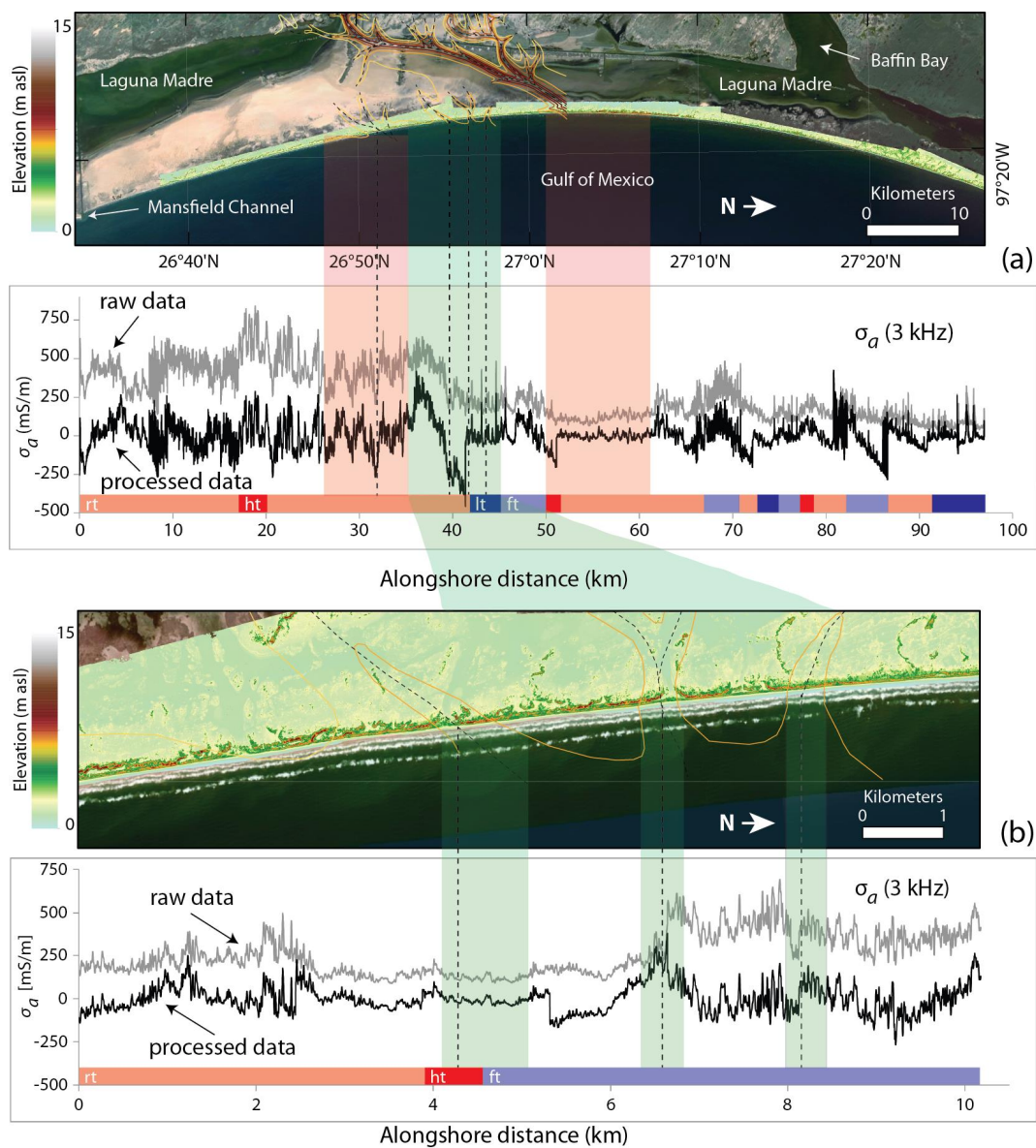
1260

1261



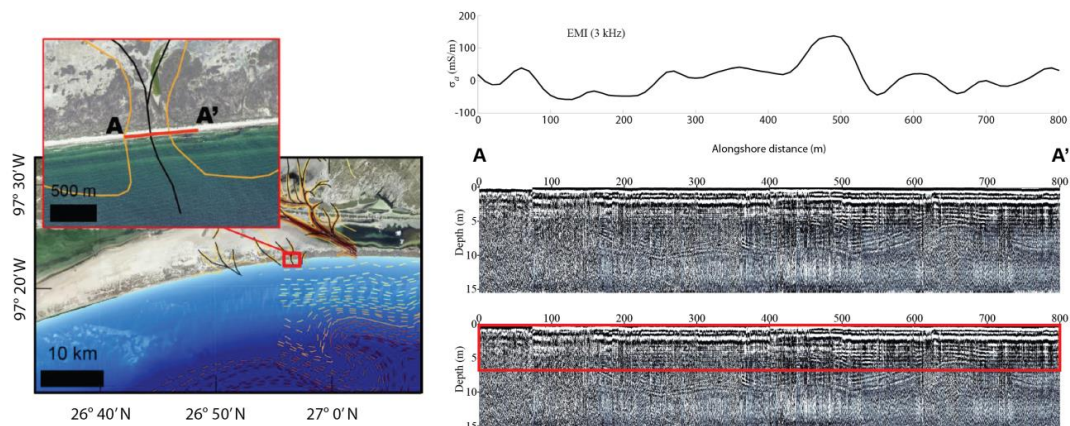
1262  
1263  
1264  
1265  
1266

Figure 1.



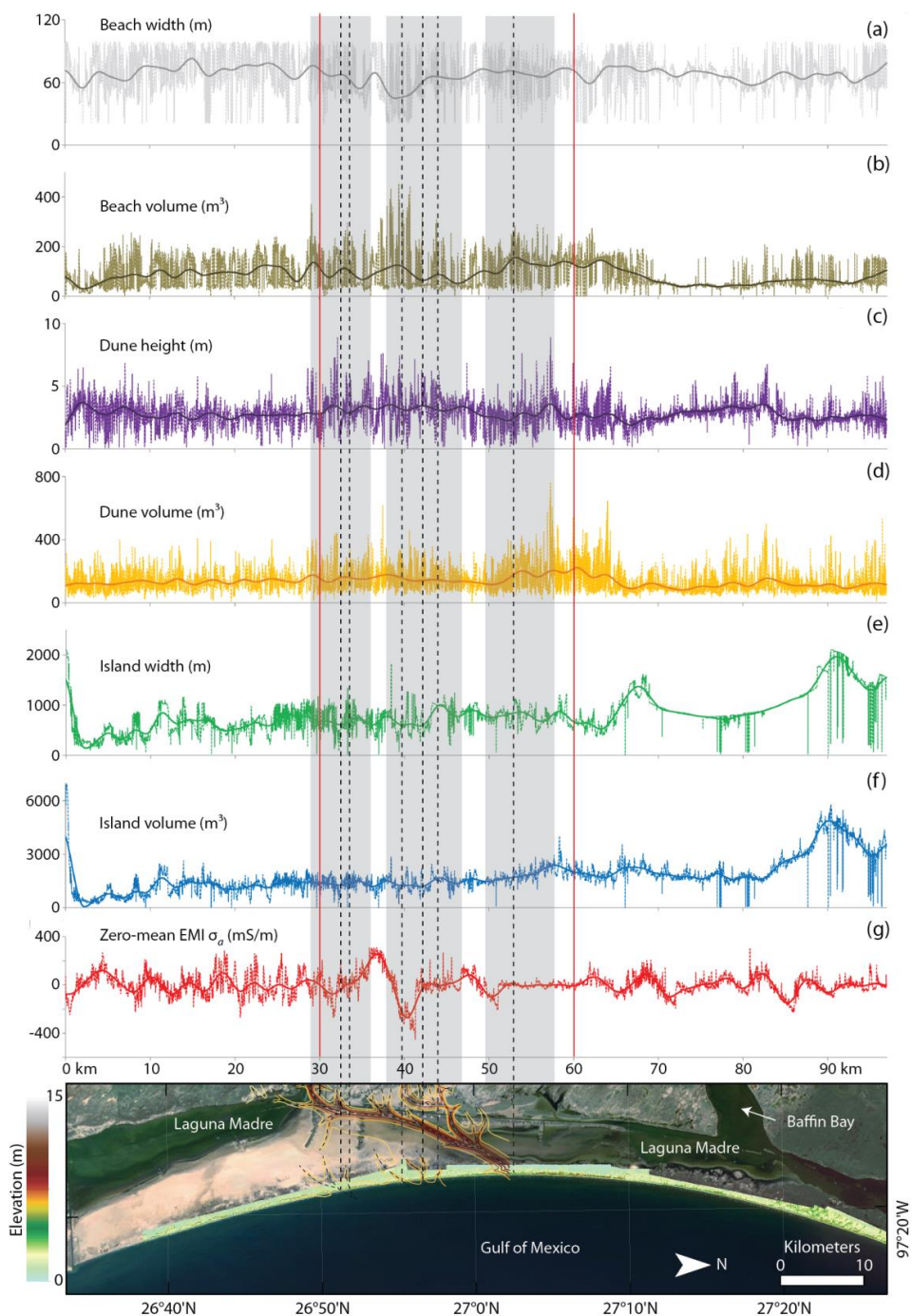
1267  
1268  
1269  
1270  
1271  
1272  
1273  
1274  
1275

Figure 2.



1276  
1277  
1278  
1279  
1280  
1281  
1282  
1283  
1284  
1285  
1286  
1287  
1288  
1289  
1290  
1291  
1292  
1293  
1294  
1295  
1296  
1297  
1298  
1299  
1300  
1301  
1302  
1303  
1304  
1305  
1306  
1307

Figure 3.



1308  
1309  
1310

Figure 4.

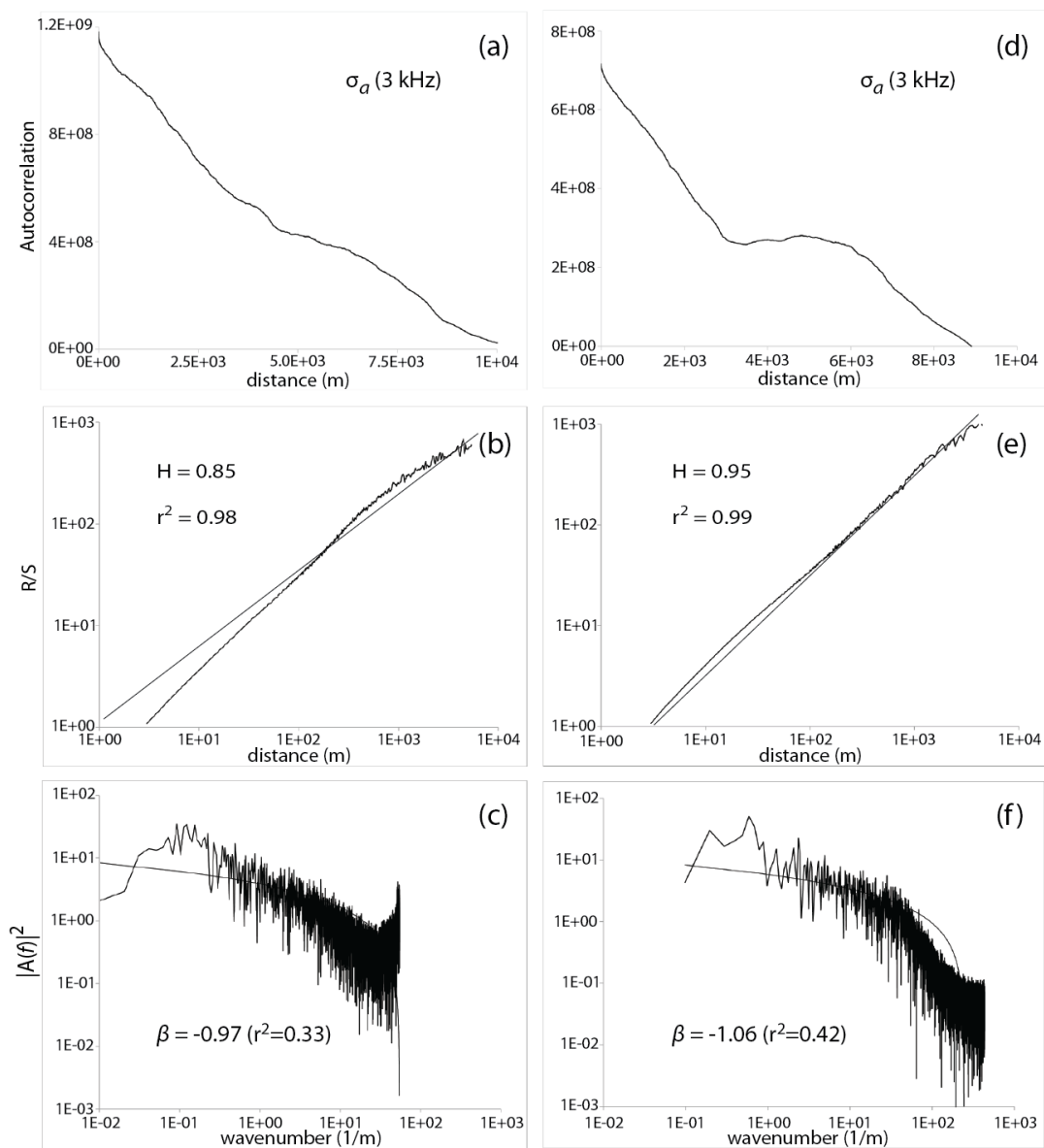
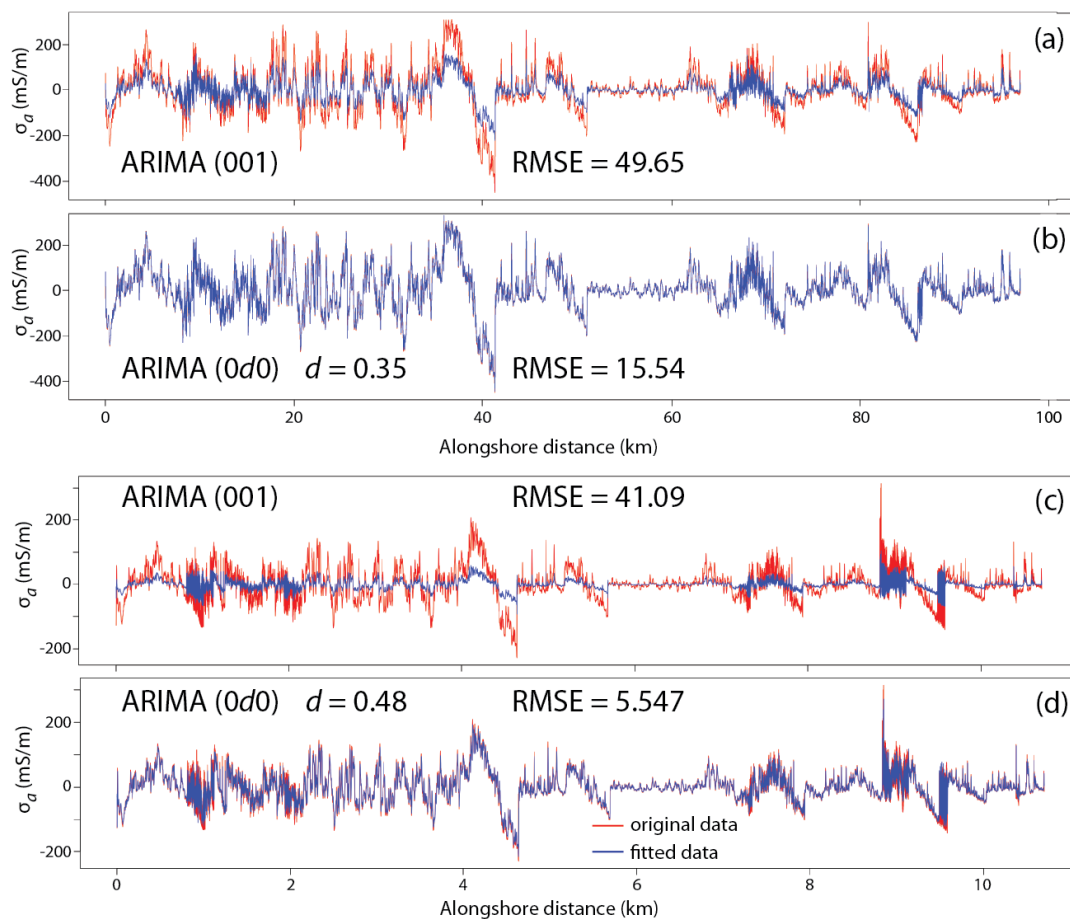


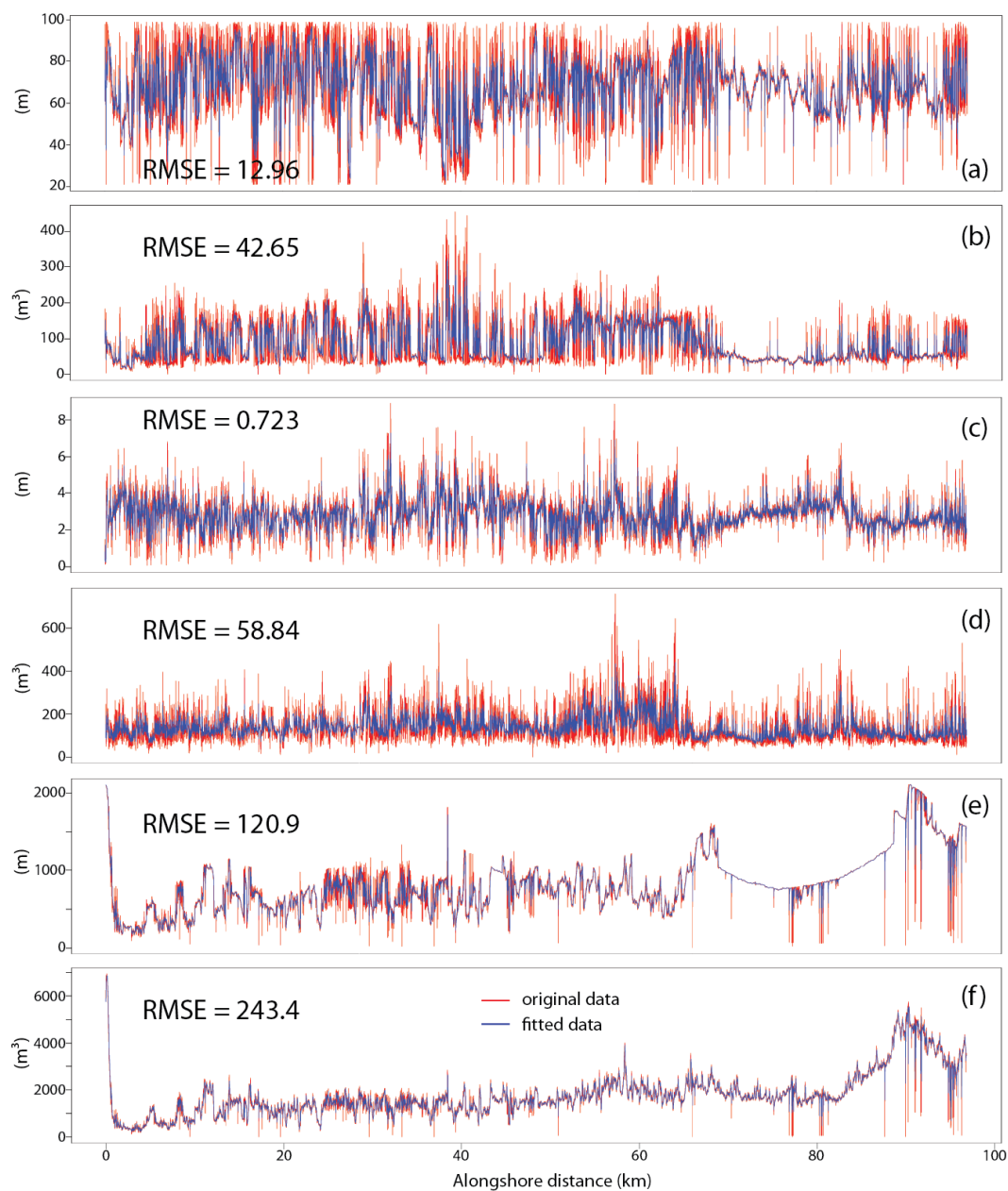
Figure 5.

1311  
 1312  
 1313  
 1314  
 1315  
 1316  
 1317  
 1318  
 1319



1320  
1321  
1322  
1323  
1324  
1325  
1326  
1327  
1328  
1329  
1330  
1331  
1332  
1333  
1334  
1335  
1336

Figure 6.



1337  
1338  
1339

Figure 7.